A comprehensive study of the river plume in a microtidal setting

A. Baldoni[1], E. Perugini[1], P. Penna[2], L. Parlagreco[3] and M. Brocchini[1]

[1] Department of Civil Engineering and Architecture (DICEA), Università Politecnica delle Marche, Ancona, Italy

[2] National Research Council – Institute of Marine Biological Resources and Biotechnologies CNR IRBIM, Ancona, Italy

[3] Italian Institute for Environmental Protection and Research (ISPRA), Rome, Italy

Corresponding author: Agnese Baldoni (a.baldoni@pm.univpm.it)

Key Points:

- Study of the generation and transport mechanisms of a river plume using optical images, numerical modeling and Particle Tracking Velocimetry
- The river discharge is the main generation mechanism determining the largest plume offshore extensions and concentrations
- Wind and waves affect the sediment dispersal to sea, defining the plume direction and the alongshore extension

Abstract

We performed a comprehensive study of the generation and transport mechanisms of a river plume flowing into a microtidal environment. First, we analysed images simultaneously acquired by both two shore-based stations and satellite and correlated the plume offshore extension with the estuarine forcing. Furthermore, we run numerical simulations to reproduce real-life events, characterized by a combination of forces, and to distinguish the role of each forcing. We identified the river discharge and the wind as the main generation and transport mechanisms, respectively. Moreover, waves were able to both generate and drag plumes. Results showed that a river discharge associated with a return period of 1 year produced a denser plume than 10-years return period waves. The transport mechanisms were responsible for the alongshore extension of the plume and consequent potential nourishment of the beaches. The tide, even if secondarily, could affect the plume evolution, depending on its phase shift with respect to the river discharge peak. Finally, we used Particle Tracking Velocimetry on videos acquired by a shore-based station to obtain the surface velocity field in the final river stretch. Such velocity was then modified to consider the effect of wind and waves, so that it could be correlated with the plume extension. The relation between the along-river component of the plume velocity and the plume extension followed a linear law with angular coefficient inversely proportional to the alongshore component of the plume velocity.

Plain Language Summary

When rivers flow outside from the estuaries, carrying sediments, they form buoyant plumes that mix with the open sea. Such plumes are key factors in the redistribution of river-borne constituents, including sediments, nutrients and pollutants, to the sea and the nearby coastal areas. Most of the studies focused on very large rivers, mainly characterized by large tidal excursions. This study, instead, investigated the fate of sediments released by the Misa River (Middle Adriatic Sea, typically with a tidal excursion of some decimeters) that, despite its small dimension, is characterized by a large sediment transport. We used multiple techniques to investigate the estuarine dynamics, like images, videos, field measures and numerical models. Such integrated approach allowed us to identify two plume generation mechanisms, i.e. the river discharge and the waves. Since the first one resuspends more material than the latter, plumes caused by river discharges release the largest amount of sediment to sea. Once out from the river mouth, the plume is transported along the coast by the transport mechanisms, mainly wind and waves, and contributes to the nourishment of beaches.

1 Introduction

When a river discharge inflows to sea, it forms a buoyant plume composed of suspended and dissolved constituents that mix into sea water. Thus, understanding of the structure, dynamics and evolution of the plumes is fundamental to comprehend the land-ocean exchanges. The formation and spreading of a river plume are governed by both "immanent characteristics" and "external forcing" (Osdachiev & Zavialov, 2019). The first group includes local topography, morphology and latitude. River discharge, local wind, tide, coastal circulation, stratification of the ambient ocean and waves belong to the second group.

Plumes have been classified as "large scale" plumes, typically dominated by rotational processes, and "small-scale" plumes, characterized by the prevalence of inertial effects and forming a freshwater bulge in the vicinity of the outflow (Garvine, 1995). Yankovsky and Chapman (1997) distinguished between "surface-advected" plumes, i.e., shallow plumes only affected by surface dynamics, and "bottom-advected" plumes, influenced by bottom Ekman dynamics and thermal wind balance.

In macro and meso-tidal environments, tides can affect the behaviour of plumes in different ways. Spring tides, in combination with wind mixing, lead to a well-mixed plume, while during neap tides and low winds, the region re-stratifies because of the relaxation of the cross-shore density gradients due to gravity (Simpson et al., 1993). Additionally, a semi-diurnal variation occurs during periods of stratification when cross-shore exchange currents become significant. Various studies focused on the effects of tidal currents on the spatial evolution of the plume. Lee and Liu (2013) observed that tides increase the horizontal and vertical mixing, especially in shallow regions, this causing a small plume extension and a reduced plume dispersal. Li and Rong (2012) found that tidal currents force the plume to move in the dominant tidal-current direction near the mouth of the river and, subsequently, the Coriolis force deflects the plume,

this causing the increment of freshwater transport.

In microtidal seas, where tidal effects are negligible, it is commonly recognized that winds are the dominant forcing driving the plume variability. The presence of winds highly affects the plume behaviour, moving the plume onshore during periods of downwelling wind and offshore during periods of upwelling wind, regardless of the direction of the ambient flow. Upwelling-wind opposes the along-shelf propagation of buoyant plumes and induces significant mixing (Fong & Geyer, 2001), causing the plume to expand offshore, thin, and eventually separate from the coast. In contrast, downwelling-wind causes the plume to narrow and thicken and the plume front to steepen. Another important finding was that seaward winds are most likely involved with the shear-produced destratification, while onshore winds, pushing a part of the plume back into the estuary, developing an advection-related destratification (Chao, 1988). Other factors affecting the evolution of plumes in microtidal environments are illustrated in Mestres et al. (2007), who demonstrated that i) the site topography strongly influences the propagation of the plume, affecting its distribution and shape; ii) even a small bottom slope increases the along-shore extension of the plume and limits the offshore one; iii) the higher the river discharge the higher both the along-shore and cross-shore dimensions of the plume. As regards the fate of suspended sediments transported by plumes in microtidal environments, the coarser particles settle in the vicinity of the river mouth and subsequently move alongshore as bedload, while the finer particles are transported more offshore because the diffusion mechanism is stronger than the settling one (Arnoux-Chiavassa et al., 1999). This behaviour is also typical of the plumes due to small mountainous rivers, which, even if less studied than the large-size rivers, can play a significant role in the supply of sediment to continental shelves (Bourrin et al., 2008).

River plumes have been widely studied through shipboard monitoring and Lagrangian drifters that, following the direction of the plume spreading, acquire physical and geochemical measurement and sample suspended matter (Broche et al., 1998; Naudin et al., 1997). Numerical modelling has also been a widespread technique for investigating the fate of river jets (a.o. Garvine, 1999; Li & Rong, 2012; Mestres et al., 2007), having the possibility also to release Lagrangian tracers and perform a particle-tracking analysis (Banas et al., 2009). In the last decades, remote sensing has been used to overcome the problems of conventional monitoring techniques. Images can supplement field data by revealing broad-scale patterns, recording changes over time, providing data for inaccessible regions, and decreasing data acquisition costs. Satellite imagery allows the monitoring of river plumes behaviour over large distances (Soosar et al., 2016), but has a limited temporal resolution and data acquisition is limited by bad meteorological conditions such as cloud cover. Drones can efficiently monitor small river plumes because they can continuously observe sea surface with high spatial resolution from relatively low altitude. This allows to describe the extremely rapid response of the river plume to forcing conditions (Liedtke et al., 1995; Osdachiev et al., 2020). However, the use of airborne monitoring systems

has some drawbacks, i.e., the short duration of continuous operations, costs, limited weight of carried instruments, and impossibility of its operation during inappropriate weather conditions (strong wind, rain, snow, low temperature). Other remote sensing approaches include synthetic aperture radar (SAR) images, used for example by Hessner et al. (2001) to recognize and interpret sea surface patterns on the Rhine plume. Finally, video and images recorded by fixed stations can be used to continuously survey the evolution of a river water plume. Morichon et al. (2008) applied image-processing techniques on video-images acquired by the Argus video system to delineate plume fronts. Despite some limitations, like the decreasing resolution of the images far from the station, the shore-based video system offers several advantages such as acquisition frequency flexibility, high spatial resolution, weak climate dependency, and low cost compared with commonly used remote-sensing techniques to operationally estimate river plumes.

The present study aims at characterizing the mechanisms responsible for the formation and evolution of a small-discharge river plume in a microtidal environment using an integrated approach, including satellite images, shore-based video-monitoring of the plume front, in-situ meteo oceanographic data acquisition system, numerical modelling and Particle Tracking Velocimetry (PTV) analyses. In more detail, we used images acquired since 2016 by two land-based video-monitoring stations placed along the same coastline at a longshore distance of about 2 km, to assess the extension of the plume and determine if it contributes to the supply of sediment to the downstream beach. In addition, we also used satellite images from Sentinel2, to have a wider visualization of the plume. Then, we correlated information derived from the images with the forcing affecting the plume evolution, this allowing us to identify different generation and transport mechanisms. Moreover, we run numerical simulations and conducted PTV analyses to further investigate both real-life cases, characterized by the interaction of multiple forcing, and the effect of single parametric forcing on the plume generation and evolution. The aspects we want to study are: i) the local generation mechanisms of the plume in a microtidal environment; ii) the extension of the plume; iii) the forcing affecting the plume evolution; iv) the potential nourishment of the beach by plume sediment.

Section 2 describes the characteristics of the studied area and of the video-monitoring stations, including the technique used to post-process the images and extract the plume extent, and outlines all the other datasets used for the analysis. The set-up of the numerical model used to simulate the plume evolution and the used PTV technique are also included in Section 2. Section 3 reports the results of field observations, numerical simulations and PTV analyses, while discussion and conclusions are given in Section 4 and Section 5, respectively.

2 Materials and Methods

2.1 Field site

The study area includes the Misa River estuary (MRE hereinafter) (Senigallia,

Marche, Italy) and the stretch of beach that extends from the river jetty to around 2 km south. The coast of Senigallia, along the Adriatic Sea in central Italy, is located in a microtidal environment (mean tidal range, TR, rarely exceeding 0.6 m and RTR=TR/Hb<1, with Hb height of breaking waves) and the coastline has a NW–SE orientation (Figure 1a) and faces approximately 40° from the north. The submerged beach to the south of the river jetty is characterized by fine-to-medium sands with a median grain size (50) of 0.125– 0.25 mm (Postacchini et al., 2017) and usually features an array of three–four shore-parallel, shallow bars within 300 m from the shoreline, in water depths between 0 and 3 m. The watershed extension of the Misa River (MR hereinafter) is 383 km2, with discharges of about 400, 450, and 600 m3 s-1 for return periods of 100, 200, and 500 years, respectively. However, reduction in the streamflows might be expected in present and future years in some regions of the Central Italy, as a consequence of climatic variability and human activities (Darvini & Memmola, 2020).

The MR behaves as other Apennine Mountains rivers: although relatively small in size, it distributes large quantities of sediment, generated by the easy erosion of the rocks that constitute the Apennine Mountains. The suspended sediment discharge from the MR is estimated to be between $4.7 \cdot 108$ kg yr-1 and $8.4 \cdot 108$ kg yr-1 (Milliman & Syvitski, 1992; Frignani et al., 2005). The sediment grain sizes throughout the MR can range from clay to cobble. The deposition of volcanic ash, transported from the southeast by winds during the Plinian and other volcanic eruptions (Pigorini, 1968; Rolandi et al., 2008), has enhanced the cohesive nature of the sediments within the MR, by adding an abundant supply of montmorillonite clay minerals (2-5 m in size). Cores of the alluvial layers that underlie the town of Senigallia, collected by Favali et al. (1995), displayed layers of muddy sediments, interspersed with gravel, all of which overlie the bedrock of fractured and faulted mud-, silt- and sandstone. Brocchini et al. (2017) found that a thick sequence of muddy sediments was present in the MR estuarine portion of the riverbed surface, with fine sands near the mouth and in the lower reaches of the MR.

2.2 Video-monitoring analysis and products

The MRE is monitored since 2015 by the Sena Gallica Speculator (SGS) station, deployed at the north pier of the Senigallia harbour within the EStuarine COhesive SEDiments (EsCoSed) project framework (Brocchini et al., 2017). SGS is composed of four cameras located on the top of a tower, 25 m above the mean sea level, and oriented to frame both the MRE and the 500 m-long unprotected beach between the harbour southern jetty and the Rotonda pier, with an overall field-of-view angle of around 200°. The surrounding nearshore region of MRE is contextually monitored by another video system (https://videomonitoraggio.isprambiente.it), deployed and maintained by ISPRA (Italian Institute for Environmental Protection and Research) in order to provide information on sand bar dynamics (Figure 1a). The monitoring stations share a similar sampling strategy, collecting images of the nearshore zone at 2 Hz for ten

minutes during each daylight hour (from 5:00 AM to 5:00 PM UTC) through digital video-cameras (Perugini, 2018; Perugini, 2019; Parlagreco, 2019).

The images collected by the SGS station have been used for a quantitative analysis, since orthorectified and stabilized time exposure (Timex) images have been used to manually track the plume front (red line in Figure 1b). A local reference system with the x-axis located in the along river direction was used to perform such analysis (blue lines in Figure 1b). The offshore extent of the plume has been computed quantitatively as the maximum distance of the plume front from the y-axis (yellow line Figure 1b).

Oblique images from the ISPRA video system (Figure 1c) were used to qualitatively correlate with the findings from SGS images and to inspect the distance reached by the plume in the southeast direction. In most cases, we found that the plume extended to the location of the ISPRA video system (2 km southward from SGS) and farther. The ISPRA images were available since May 2016 and for a limited period of time (May-November 2016) cameras were oriented toward the MRE, allowing a better visualization of the alongshore extension of the plume.

Satellite images confirmed the large spreading of some plumes. In fact, satellite imagery from Sentinel-2 was useful to observe the plumes over several years and within a wider area. The available tiles were 100×100 km2 ortho-images in UTM/WGS84 projection and had a temporal resolution of 5 days. The satellite images have been used to track the front of the plume and determine its extension applying the same procedure and shoreline reference used for the SGS images.

The information derived from the images has been correlated with the forcing typically involved in the evolution of a river plume, described in the next paragraph: river discharge and water level, wind speed and direction, sea current magnitude and direction, sea and tidal level and wave climate.

2.3 Data collection

River water levels were measured by six hydrometers deployed along the Misa and Nevola (a tributary of the MR) rivers and managed by the Italian Civil Protection – Marche Region. The locations of such hydrometers are shown in Figure 2a: H1 (Ponte Garibaldi) and H2 (Bettolelle) are downriver of the convergence of the MR with the Nevola river, H3 (Pianello di Ostra) and H4 (Serra dei Conti) are along the mountain stretch of the MR while H5 (Passo Ripe) and H6 (Corinaldo) are along the Nevola river. Figure 2b reports the data when each hydrometer started working. The integration of multiple hydrometers was needed to compensate for possible lack of data.

Data of river discharge were obtained using the rating curves of "Bettolelle", located about 10 km upriver of the MRE (H2 in Figure 2a), which acquires a datum of river water level every 30 minutes and cannot register valid data when the water level is too low (0.7 m). Since we needed a complete dataset to be used as input in the numerical simulations, we built a continuous water level timeseries by setting the missing values of water levels equal to the minimum validated water level and computed the river discharge through the rating curves.

Wave climate data (wave significant height, peak period and direction) were collected by an offshore ADCP located within the Meda station, which is about 1.5 nautical miles north of Senigallia and 1.5 nautical miles offshore. The ADCP was installed within the MORSE project (http://www.morse.univpm.it) in

August 2018 and is managed by the CNR-IRBIM (National Research Council – Institute of Marine Biological Resources and Biotechnologies). For previous periods, the wave climate was derived from a multi-year wave hindcast from the Mediterranean Sea Waves oceanographic model by the E.U. Copernicus Marine Service (CMEMS) (Korres et al., 2019). Hourly-averaged values of significant wave height s, peak period p, and main wave direction have been collected at the model node closest to the Meda station, at a water depth of around 10.5 m.

The sea water level was derived from a tide gauge installed during the MORSE project within a protected area close to the entrance of the Senigallia Harbour in 2018. For earlier periods, we used online data acquired by the ISPRA Tide Station located inside the Ancona Harbour, about 25 km away from Senigallia. The two signals are in good and continuous agreement. The Ancona and Senigallia tide gauges record water level data every 10 and 6 minutes, respectively, and their elevation datum is the mean sea level. In addition, the astronomical component of the tide was derived from the total signal recorded by the Ancona gauge using the tidal analysis of Deft3D Tide module.

Data of speed and direction for both wind and current were provided by the Meda TeleSenigallia station (Ravaioli et al., 2007), located about 2 nautical miles north and 1.5 nautical miles offshore from the harbour of Senigallia and managed by CNR-IRBIM. Data resolution is one datum every 10 minutes. The Sontek XR Acoustic Doppler Current Profiler was installed in May 2016. The current data of a 3-meter cell, positioned between 7 and 10 meters from the bottom, were averaged by the instrument during the sampling phase. Being the seabed at a depth of 12.5 m, these data are the most superficial ones.

2.4 Numerical simulations

Hydro-morphodynamic simulations were performed using the Delft3D software suite (Lesser et al., 2004; Deltares, 2014; Deltares, 2019), a widely used 3D modeling suite to investigate hydrodynamics, sediment transport and morphology for fluvial, estuarine and coastal environments. A two-dimensional (2D), depth-averaged, model was implemented coupling the FLOW and WAVE modules. Two regular grids, made by rectangular elements aligned with the coastline and the river axis, were created (*Figure 3*). As standard for Delft3D, in the WAVE computation, the finer grid was nested into the larger grid, whereas in the FLOW computation, the domain decomposition approach was used. The larger grid covered the coastal area in front of the Senigallia Harbour, it had a spatial resolution of 33.3×33.3 m^2 and extended about 7.8 km in the alongshore direction and 2.5 km in the offshore direction. The finer grid covered the final stretch of the MR and extended southwards reaching the beach in front of the ISPRA video system. It had grid cell size variable from around 8.3 m in the offshore region to around 3.0 m along the river and it extended about 2.5 km in the alongshore direction and 0.8 km in the offshore direction. The reference system used for the simulations was Monte Mario / Italy Zona2.

We performed a model calibration and two real-life simulations by on-

line coupling Delft3D-FLOW with Delft3D-WAVE, forcing the model with the real field conditions described in Section 2.3. For the WAVE model, the seaward boundary of the larger grid was forced using time-series of wave parameters. For the FLOW model, a total of four boundaries were defined. In the finer grid, a total discharge boundary condition was used in the upstream boundary of the river channel (*Figure 3b*). In the same section, a cohesive sediment concentration was imposed

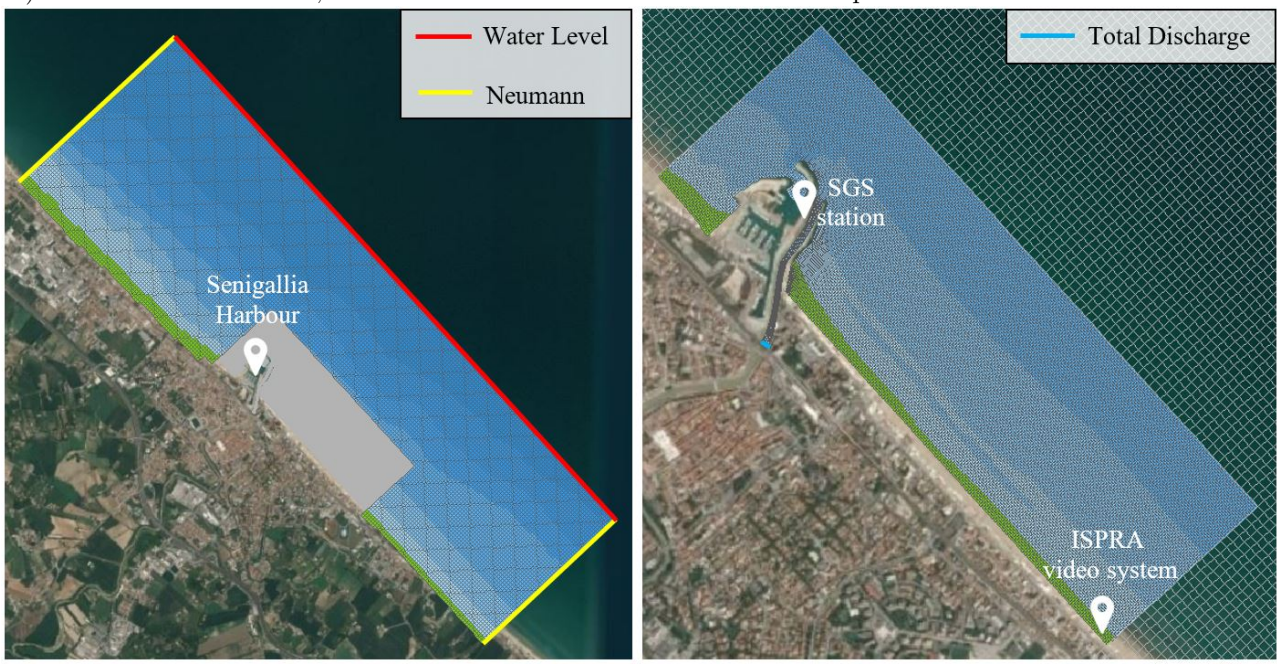

defined in Section 2.4.1. In the larger grid, the offshore boundary was forced with a water level timeseries, using data recorded by either the Senigallia or the Ancona tide gauges depending on their availability. At the two cross-shore boundaries, zero-gradient water level (Neumann-type) boundary conditions were specified (*Figure 3a*). Moreover, wind timeseries, uniformly distributed over the domain, were used as input forcing. We chose not to implement marine currents due to the Adriatic global circulation (e.g. Western Adriatic Currents) because the available data were acquired 1.5 nautical miles offshore from the MRE and, displaying a decreasing intensity toward the shoreline, would represent a secondary agent for the plume evolution. Finally, we considered a background concentration for the Northern Adriatic Sea equal to 0.05 kg/m^3 (Harris et al., 2008; Brando et al., 2015).

The bathymetry was created by interpolating at the grid nodes the depth values coming from both the EMODnet bathymetry, available online, and some multibeam echosounder surveys performed in the estuarine area. For the model calibration, which reproduced an event occurred in 2014, we used a survey carried out in January 2014. For the two simulated real-life cases, occurred in 2019,

the survey in use was that of 2018. The bed stratigraphy was modelled using one mixed layer composed of a space-variable mix of fine sand and cohesive sediment. Based on in situ samplings (Report – Marche Region, 2020), the upper stretch of the MR was characterized with 100% cohesive sediments, then, the presence of silt and clay decreased seaward until reaching 100% of sand in the sea area. A 12-hour spin-up interval, during which the model did not perform any morphological update, was used.

2.4.1 Assessment of the model performances

We reproduced a real-life event occurred in January 2014 for which some turbidity measures along the MR were available (Brocchini et al., 2017; Postacchini et al., 2021). Such turbidity measures were converted to concentration measures using a conversion factor of 1 NTU = 10 mg/l (Postacchini et al., 2021). We run a simulation from 24 January 2014 to 29 January 2014 and compared the results in terms of suspended sediment concentration with the field measurements. The depth-averaged velocities resulting from the simulation had already been validated in Baldoni et al. (2021). The plume was the result of both sediment transported by the river from the upstream part of the basin to the mouth and sediment suspended locally in the final stretch of the river by the river current and the waves. For that reason, an input concentration was used at the upstream boundary of the river channel in this calibration and in the real-life cases. Such concentration was chosen to be proportional to the river discharge through a factor of 1/3, which is a reasonable value for the MR. We derived such value after an analysis on the sediment transport for the rivers of the Marche Region, carried out using the data provided by Aquater (1982). We computed the mean annual suspended concentration for several rivers using such data and we assumed that the transport capacity of the rivers remained unchanged over the last years. Thus, we hypothesized that the suspended concentration transported by the rivers remained unaltered and that the concentration could be taken as proportional to the river discharge. We performed such analysis for several rivers of the Marche Region for the year 2014 and we obtained concentration-to-river-discharge proportionality factors in the range 1/1.2 to 1/7. This reasonable simplification, least accurate for the initial phases of the flood hydrograph (when liquid and solid discharge are not yet proportional), allowed us to estimate an input concentration. *Figure 4* shows the modelled cohesive suspended concentration in red and the measured concentration in blue. Our model well reproduced the decrease of the concentration toward the sea, due to the dilution of the freshwater with the sea water. Also, the modelled quantity of suspended sediment was of the same order of magnitude of

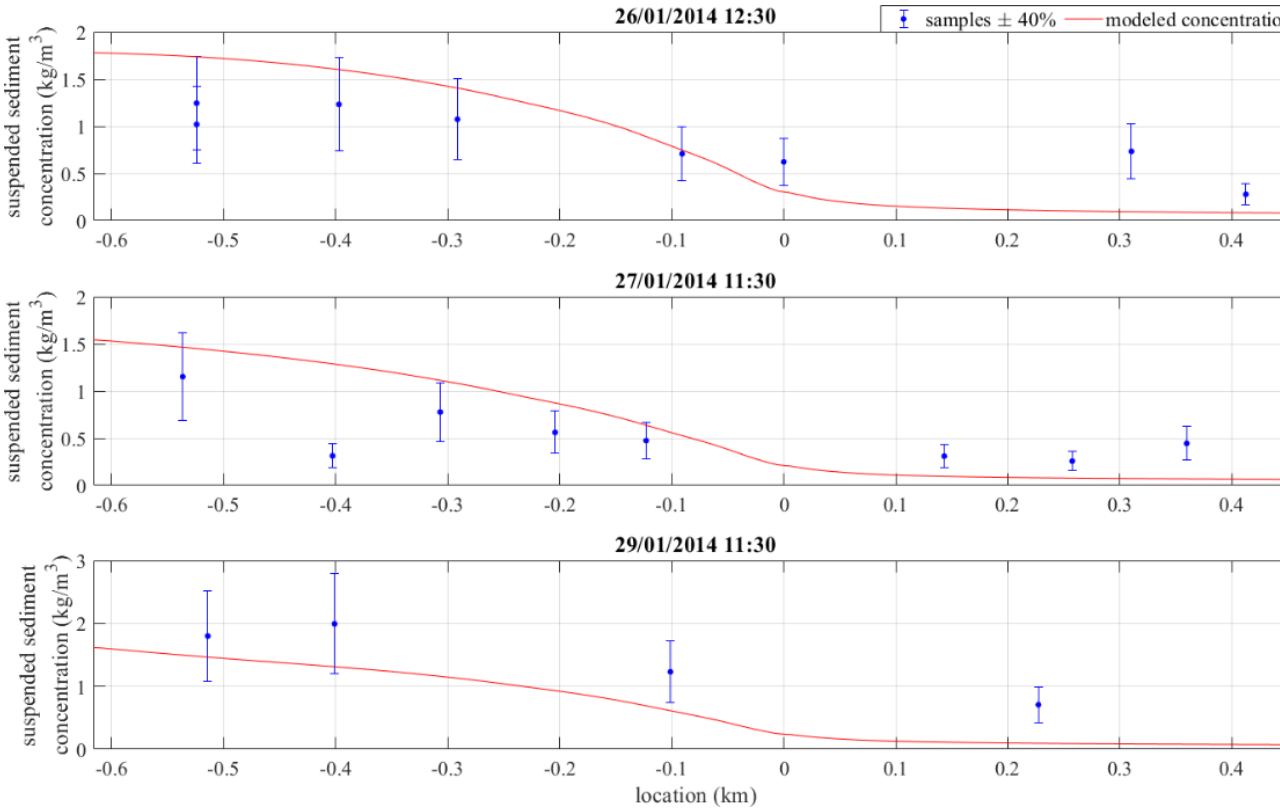

measured one.

2.5 PTV analysis

Particle Tracking Velocimetry (PTV) was applied to video-frames acquired by one of the cameras of the SGS station, previously processed to best adapt to the requirements of PTV analysis. We used PTV to measure velocities of floating objects visible in the last stretch of the MR. Such objects could be either wood debris or fine material, not always preserving the same shape during the period of the analysis and possibly being temporarily submerged by the waves. Thus, our "field" images did not satisfy the traditional standards for PTV analysis, which requires well-defined bright particles against a clean, dark background. Therefore, after choosing the videos we wanted to analyse by searching for the ones displaying visible floating objects, we extracted and orthorectified the frames. Then, we pre-processed the frames using image-processing techniques to make them suitable for the PTV analysis. We converted the RGB images to grayscale and we applied the Matlab function Fibermetric to highlight tubular or elongated shapes, this allowing us to emphasize the visibility of the floating material. After switching the colours between background and foreground, setting a dark background and a bright foreground, we enhanced the contrast of the images. By choosing a suitable range of colours, the floating material could

be further highlighted, and the noise produced mainly by wave breaking could be reduced. However, some disturbances due to waves and water ripples remained. Finally, we processed the frames using the MATLAB software package Part2Track, developed at the Institute of Mechanics and Fluid Mechanics at the TU Bergakademie Freiberg (Janke et al., 2020). During the tracking operation, the software calculated the particles displacement through some user-defined parameters (e.g., particle size and brightness, field of search, etc.) and incorporated an outlier detection to enhance the quality of the displacement field reconstruction. The results by running Part2Track were a list of scattered velocity vectors for each computed frame and trajectories of the detected particles. Interpolation of the scattered data on a regular grid provided the surface velocity field. The conversion from pixels and frames to meters and seconds was performed directly by the software using the scale factor mm/px and the time separation between frames, both provided by the user.

3 Results

We performed a detailed and continuous analysis for the year 2016, when also the ISPRA cameras were looking toward the river mouth. We correlated the occurrence and extension of plumes derived from the images with the data presented in Section 2.3 to identify the main generation and transport mechanisms. We classified the plume events depending on their generation mechanism and assessed also the forcing affecting their evolution. *Figure 5* reports an example of such procedure, where the red, blue and green rectangles highlighted three plume events, generated by NNE waves only, a combination of river discharge and waves and E waves only, respectively. Moreover, we identified on the images the main characteristics of each type of plume. At the end of the analysis, we were able to distinguish two generation mechanisms (see Section 3.1), the river discharge and the waves, and some mechanisms of sediment transport (Section 3.2), the wind, the waves and the currents. Then, also using satellite images, we extended the analysis to other years and, finally, we selected two events that highlighted well the identified mechanisms.

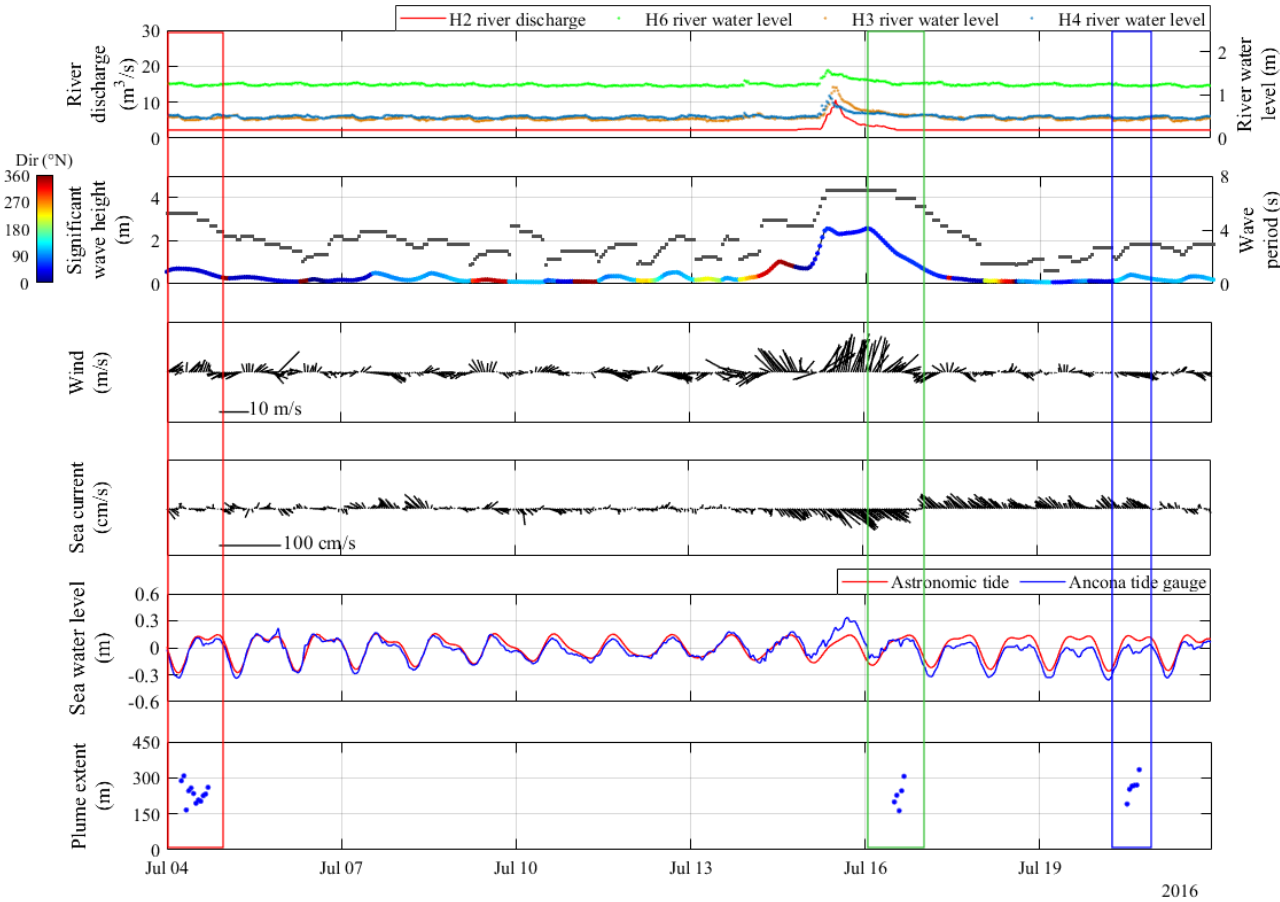

Generation mechanisms

Two main mechanisms for the plume formation, i.e. mechanisms that directly put the riverbed sediments into suspension, were recognised: the river discharge (RD) and the waves (W).

The occurrence of a river discharge was always followed by a dense plume flowing out from the estuary mouth (*Figure 6a*). Such plume appeared well marked in the images and we could recognize it clearly, since it caused a marked change in the water colour from blue to brown. Moreover, we could observe that, during this type of event, some floating woody material was frequently visible on the river water surface. Some of the videos presenting this characteristic were analysed with the Part2Track software (see Section 2.5). The high sediment concentration likely derived from both the material eroded and transported by the river from the upstream part of the basin to the mouth and from the local sediment suspended by the action of the river discharge.

Wave-forced events due to waves coming from N and NE, which easily entered the estuary, were caused by the important stirring action of the riverbed

sediments at the river mouth. Wave-forced plumes were characterized by a smaller sediment concentration than RD plumes. These plumes appeared diffused around the river mouth, frequently assuming an arcuate shape (*Figure 6b*). Easterly waves, instead, were likely responsible for resuspending the sediment in the area between the south pier of the MR and the adjacent beach, this probably causing the change of water colour along the jetty observed from the SGS images (*Figure 6c*). Also these waves could enter the MRE and weakly resuspend the sediment inside the river mouth: we observed a light change of the water colour also inside the estuarine channel. Therefore, we believe that these events are not pure plume events, but mixed events, generated by wave resuspension of both nearshore sediment and river sediment.

Plume events forced by waves (W) often generate during storms that involve both the sea and the land area, therefore the plume visible on the river mouth can often be due to combined actions of river discharge and waves, this complicating our analysis. Thus, we chose to examine more than one year to identify events that highlighted the prevalence of a single generation mechanism. In any case, when the MR plume exited the river mouth it was outside of the closure depth of the beach, estimated by Melito et al. (2020) to be around 300 m, which was the distance of the outermost sandbar from the shoreline.

3.2 Transport mechanisms

Wind, waves and sea currents were the factors affecting the plume direction, i.e. the transport of the already suspended riverbed sediments.

Waves coming from NNE, typically associated with winds blowing from the same direction, approached the coast nearly perpendicularly and caused a reduction in the offshore extension of the plume. We could observe that in cases when a river discharge occurred simultaneously with a NNE storm event, the plume

was kept inside or just outside the MR mouth until the storm decreased (*Figure 7a*). Then, as the storm passed, the river prevailed over the waves and the plume expanded into the sea (*Figure 7b*). Waves coming from E, associated with winds blowing form the same sector, normally triggered currents directed from SE to NW, this causing the suspended sediment to flow toward NW, as visible in *Figure 7c*.

Only few cases were observed characterized by winds blowing to the offshore for a long period and maintaining the same direction (about 210°N) and high speed (10-15 m/s). In these cases, conversely to what happened with winds directed toward the coast, the plume was pushed to the offshore.

Moreover, the Western Adriatic Current (WAC), described in Grilli et al (2005), likely affected the plume evolution. However, since the MR plume usually extended for less than 1 km from the shoreline, the effect of the WAC was minor. Some measurements of sea current were available at 1.5 nautical miles from the coast, recorded by the Meda TeleSenigallia station. The sea current, wind and wave directions were mostly in good agreement, and all contributed to deflect the plume toward either one direction or another. In cases when winds and sea currents were discordant, we observed that the plume typically followed the wind direction rather than the current one (see Section 3.3).

3.3 Real-life cases: observation and simulation results

We present results for an event generated by a river discharge (RD case) and an event generated by waves coming from NNE (W case), combining the observed data and the numerical simulations. It is clearly difficult to associate real-life events purely to one single mechanism, as often they are the outcome

of a combination of physical phenomena. The events described in this section are, therefore, those that were characterized by the prevalence of one generation mechanism over the others. Parametric events, modelled using one single prevailing forcing, are discussed in Section 4. We chose the two events here analysed by first defining a pool of events well visible in the images of SGS, of the ISPRA video-system and of the satellite. Then, from the above pool we selected two events that presented and highlighted the characteristics of the generation mechanisms described above. Finally, we run Delft3D numerical simulations forced using recorded timeseries (Section 2.3 and Section 2.4), which are reported in *Figure 8* and *Figure 10*, to find the concentration corresponding to the plume front.

3.3.1 RD Case

The selected plume event occurred on 29-31 May 2019 and was generated by a river discharge that reached 106 m^3/s on 29 May 2019, at 6:30 PM (*Figure 8*). The wave climate was mild, with a maximum significant wave height of 0.91 m and variable direction, mainly N and NE.

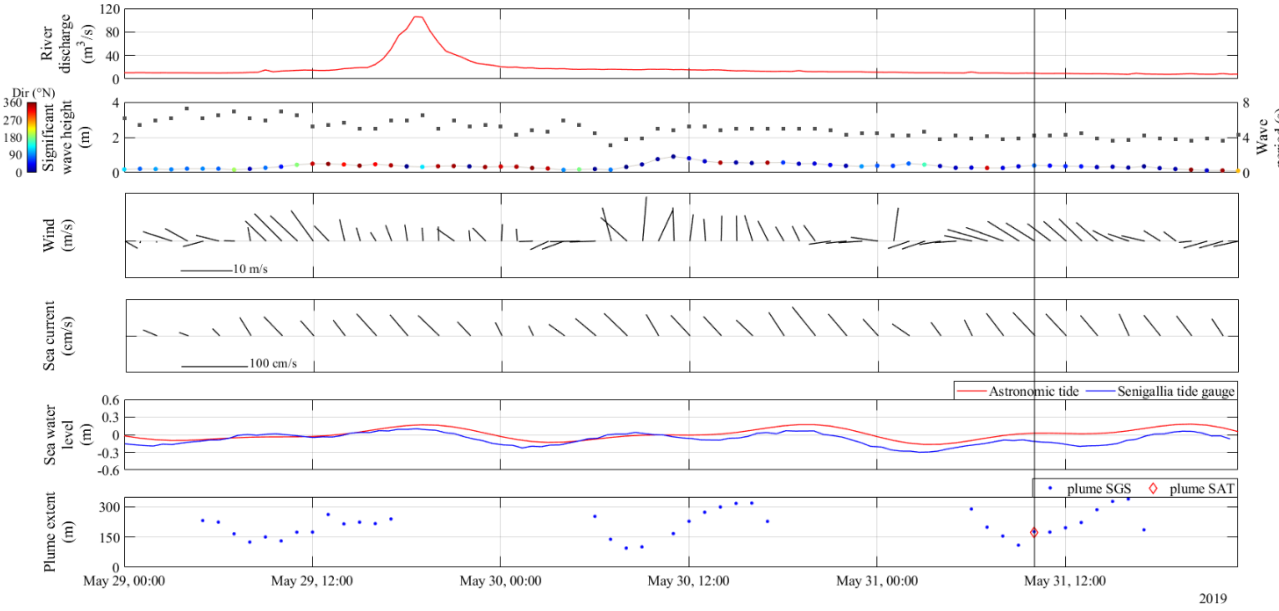

all plumes generated by a river discharge, this plume appeared dense with sediment. *Figures 9a* and *9c* show the plume from the SGS Timex image and from the satellite image, both acquired on 31 May 2019, at 10:00 AM and 10.08 AM respectively. Since this plume occurred about two days after the discharge event, a large quantity of sediment had already been washed out from the estuary, as confirmed by the bright area extending parallel to the coast. However, a dense plume could be distinguished from the background, meaning that the effect of the river discharge was still important after two days. Thus, the plume fronts drawn on the SGS and satellite images (respectively, yellow

and red lines in Figures *9a* and *9c*) identified the denser plume occurred on 31 May 2019, showing a good overlap.

After generation, the SGS images (also those of 29 and 30 May 2019, not reported here) showed the plume directed toward SE, this meaning that the prevailing transport mechanism was the wind coming from N and NNE (third panel of *Figure 8*). The current, directed toward NW, did not affect the plume direction in this case. As typically observed, the sea current intensity, measured 1.5 nautical miles offshore from the shoreline, decreased approaching the coast and was not intense enough to deviate the plume.

Figure 9d shows the map of the suspended sediment concentration (dominated by the cohesive fraction, as illustrated in the Discussion) obtained from the numerical simulation. The modelled plume deflected toward SE, as clearly shown by the images. The SGS plume front followed the 0.1 concentration isoline, while the satellite plume front fell between the 0.07 and the 0.1 isolines. Such isolines reached the nearshore region in front of the ISPRA video system. *Figure 9b*, reporting the ISPRA Timex image, confirmed that the sediments were transported

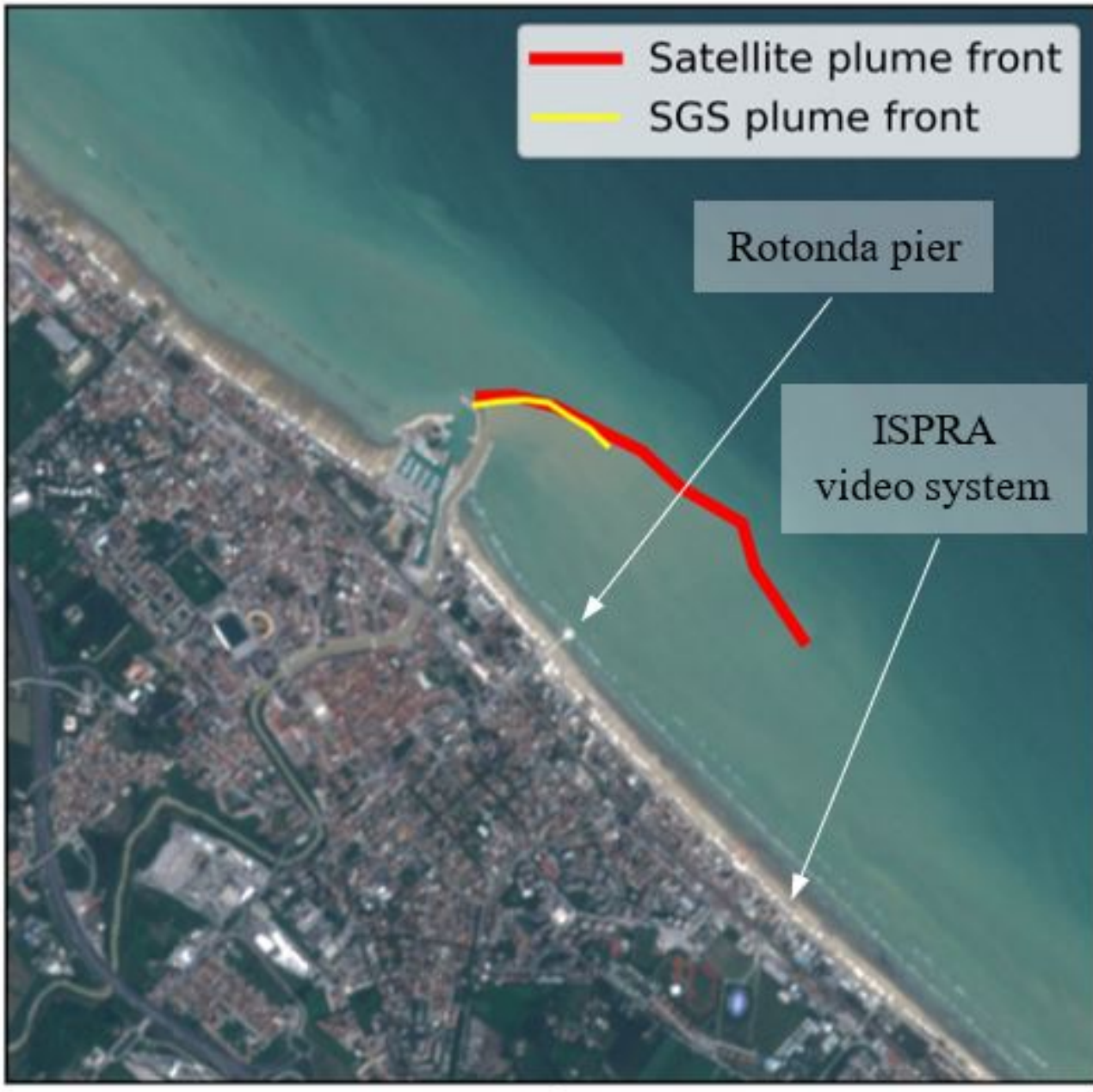

to such location well outside the breaking zone.

3.3.2 W Case

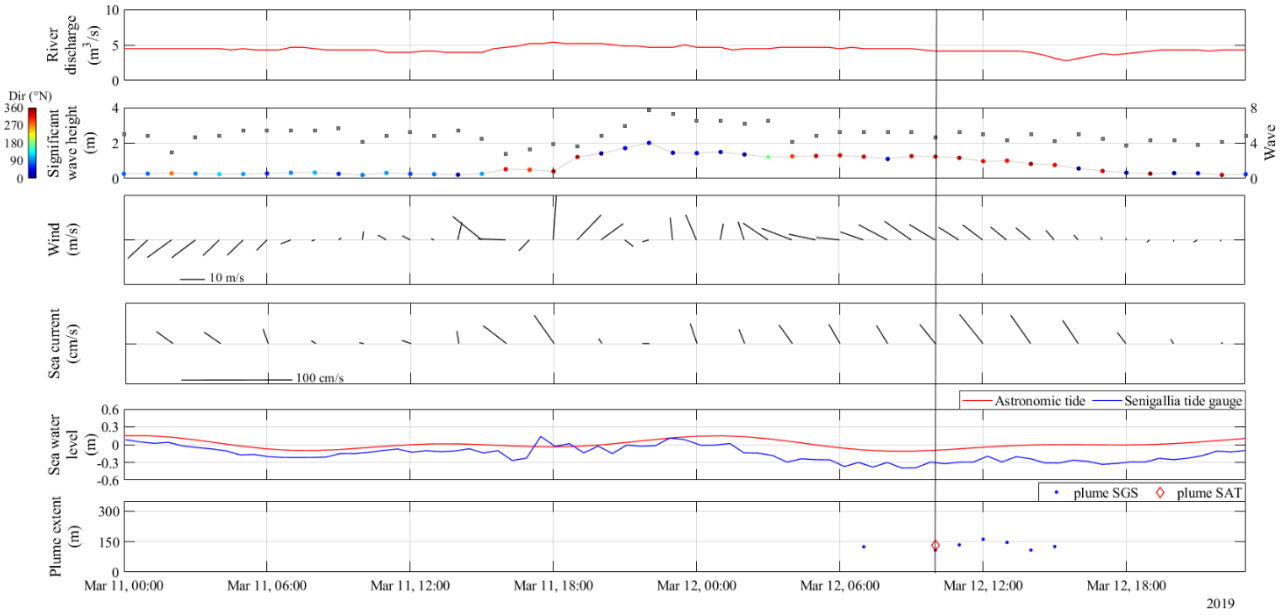

selected plume event occurred on 11-13 March 2019 and was characterized by a low river discharge of about 5 m^3/s and by N-NNE waves reaching 2 m on 11 March 2019 at 10:00 PM (*Figure 10*).

The sprays suspended by the storm caused the ISPRA images of this event to be poor in quality, thus it was not reported here. The river plume appeared less intense and it mixed with the sand resuspended by the waves in the breaking zone (*Figure 11b*). *Figure 11c* shows the suspended sediment concentration map resulting from the simulation. The high concentrations near the shoreline were caused by the resuspension of the sand due to the wave action, while near the river mouth the plume was mainly composed by cohesive sediment. The simulation confirmed the lighter density of the plume than that generated by the river discharge, the plume front falling in correspondence of the 0.059 concentration isoline, that is about a half than the value found for the RD case and quantifying the marked density difference of the two types of plumes. The two plume extensions computed from the SGS and the satellite images well overlapped (sixth panel of *Figure 10*). The W plume offshore extent was around 30 meters smaller than that of the RD case. On 12 March 2019 the wind came from NNE and, as in the RD case, prevailed on the current, deflecting the plume slightly to SE.

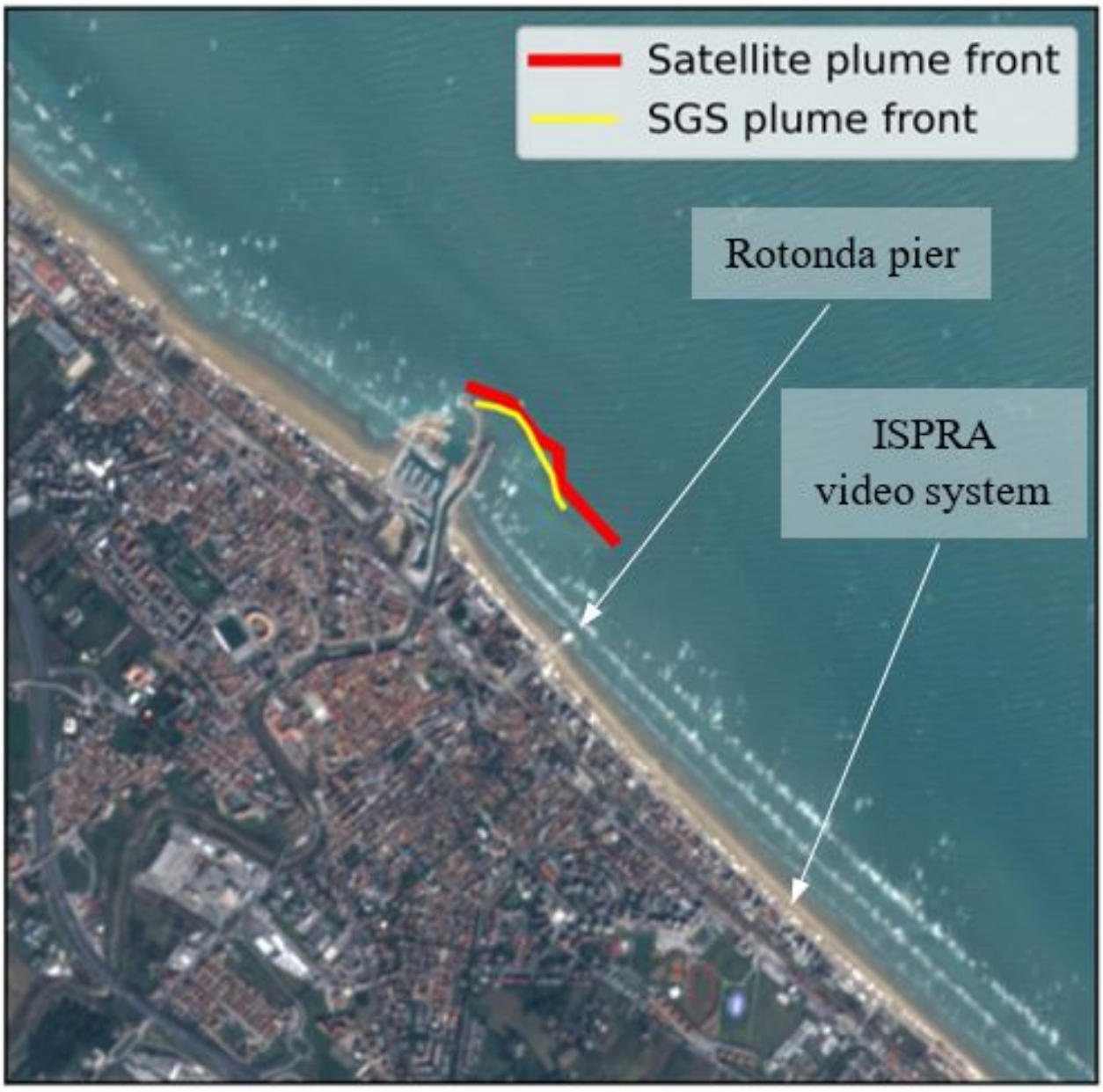

3.4 PTV results

To study the complex dynamics of the MRE, characterized by a combination of forces, we conducted PTV analyses on some videos. Among all the available data, we selected events where floating material, detectable by the PTV, was clearly visible on the river surface (*Table 1*).

Table 1. List of the analysed videos and forcing: the river discharge (Q), the wave parameters (Hs, Tp and wave dir.), the wind speed and direction (wind speed, wind dir.) (see Section 2.3). The wave parameters (significant height, peak period and direction) were transferred to the river mouth through the Delft3D wave module.

video ID	**video date**	**Q**	**H_s**	**T_p**	**Wave dir.**	**Wind speed**	**Wind dir.**
		m^3/s	m	s	°N	m/s	°N
EV1	23 Mar 2016 11 AM	81.50	1.67	7.37	44.13	12.7	16.8
EV2	25 Apr 2016 10 AM	18.44	1.44	5.74	39.64	8.31	357
EV3	02 May 2016 11 AM	32.95	0.54	5.74	18.55	5.23	313
EV4	20 May 2016 02 PM	18.44	1.03	5.07	35.22	5.96	339
EV5	20 Jun 2016 04 PM	22.79	0.42	4.47	17.37	5.15	299
EV6	07 Mar 2017 12 PM	70.36	1.51	6.5	40.43	9.86	308
EV7	03 Feb 2018 08 AM	29.47	0.85	6.5	32.99	10	300
EV8	21 Mar 2018 09 AM	49.92	1.6	7.37	42.31	13	214
EV9	14 May 2019 09 AM	17.63	1.55	8.35	45.11	4.65	31.9

Each video was about 10 minutes long but, in some cases, the floating material was visible for a shorter period, thus we analysed only the interval of frames displaying it. Moreover, we applied a mask on the frames to cover the jetties and, in some cases, also the stretch of river most disturbed by the waves. *Figure 12* displays the surface mean velocity field computed by Part2Track (Section 2.5) for EV4 and EV2 and the two different masks are identified with cyan lines. The represented velocity field was interpolated onto a regular grid built on the image.

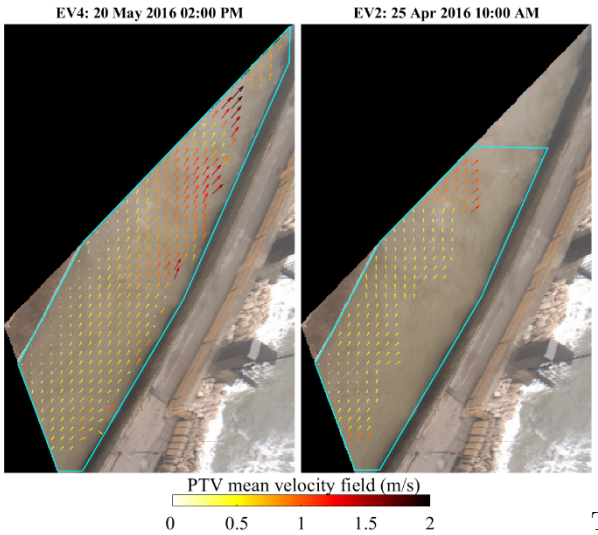

To extrapolate a single representative value of velocity for each video we computed a weighted mean of the ve-

locity field, using as weights the number of particles detected by the Part2Track algorithm in each grid cell. Such value, hereinafter named "PTV velocity", was compared with a "manual velocity" that indicated the mean velocity of some particles that we manually tracked on each video. The "manual velocities" were used to check the accuracy of the PTV results, which were characterized by a relative error in the range 0.8-33%. *Figure 13* shows the "PTV velocity" and the "manual velocity" with dots and asterisks, respectively, and their correlation with the river discharge. The surface velocities increased with the river discharge through a nonlinear, parabolic dependence ($v = -0.00027Q^2 + 0.067Q - 0.037$). The data scattering was due to the several forcing that acted in the estuarine area, e.g. wind, waves and tide, and that affected the surface velocity.

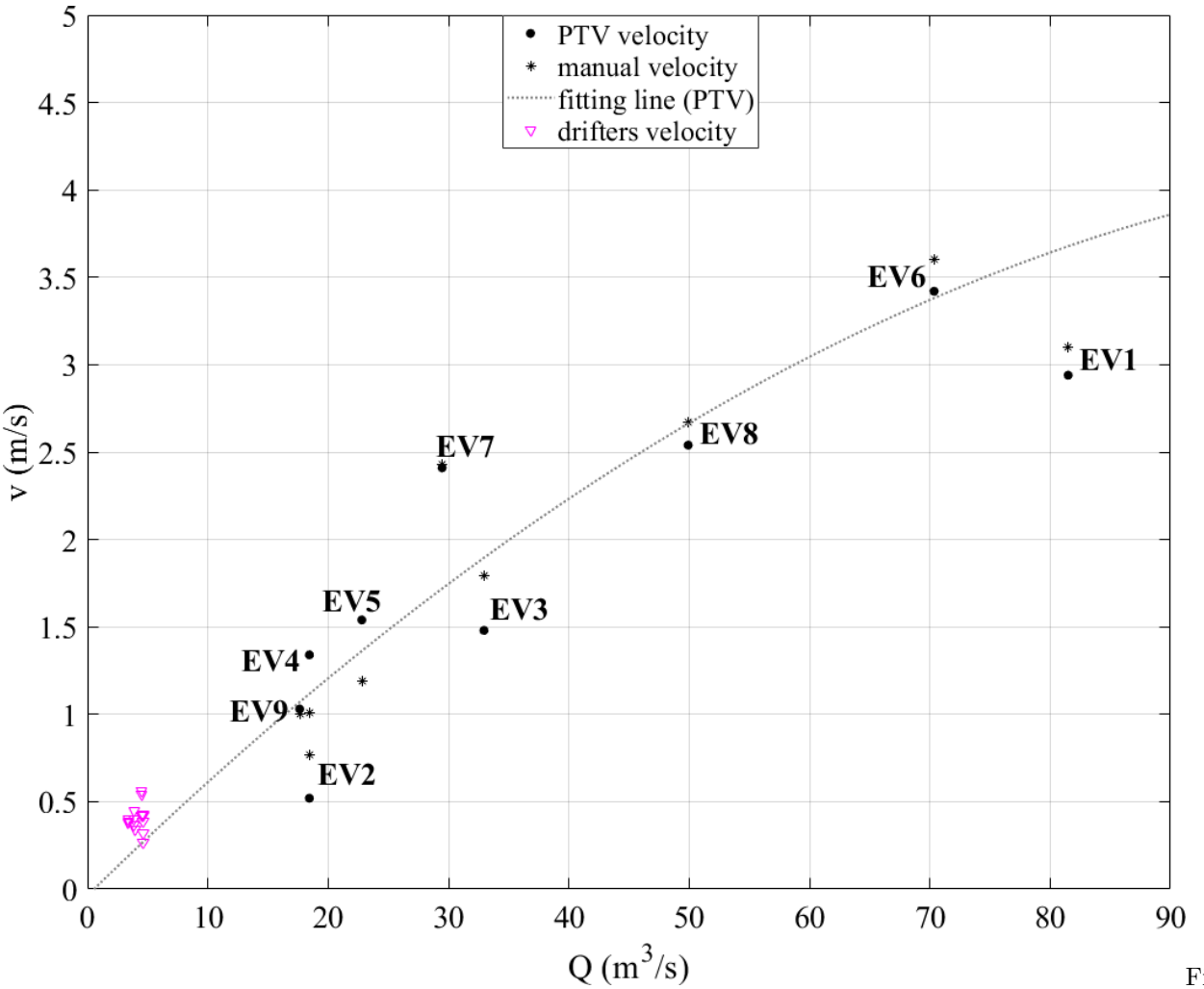

Fina

we computed the mean velocities of some drifters, launched within the EsCoSed project in 2014 (see Brocchini et al., 2017), to compare their values with

the PTV ones. The mean calculation was limited to the part of the drifters trajectories that fell within the area framed by the video-images. Such values (triangles in *Figure 13*) showed a good agreement with the fitting line, confirming the reliability of the PTV analyses.

4 Discussion

Field observation allowed us to identify both plume generation and transport mechanisms. In a natural environment, the action of a specific forcing is difficult to isolate since typically the observed physical phenomena are the outcome of a combination of several mechanisms.

To inspect the role of the different generation mechanisms separately one from another, we run parametric simulations using artificially built conditions reproducing the shape of typical flood hydrographs and storms (see *Figure 14* and *Figure 15*). For the wave direction we chose NNE and E, being the most frequent storms impacting on the Senigallia coast from these directions. At the offshore boundary a zero-water level condition was imposed to neglect the effect of the tide.

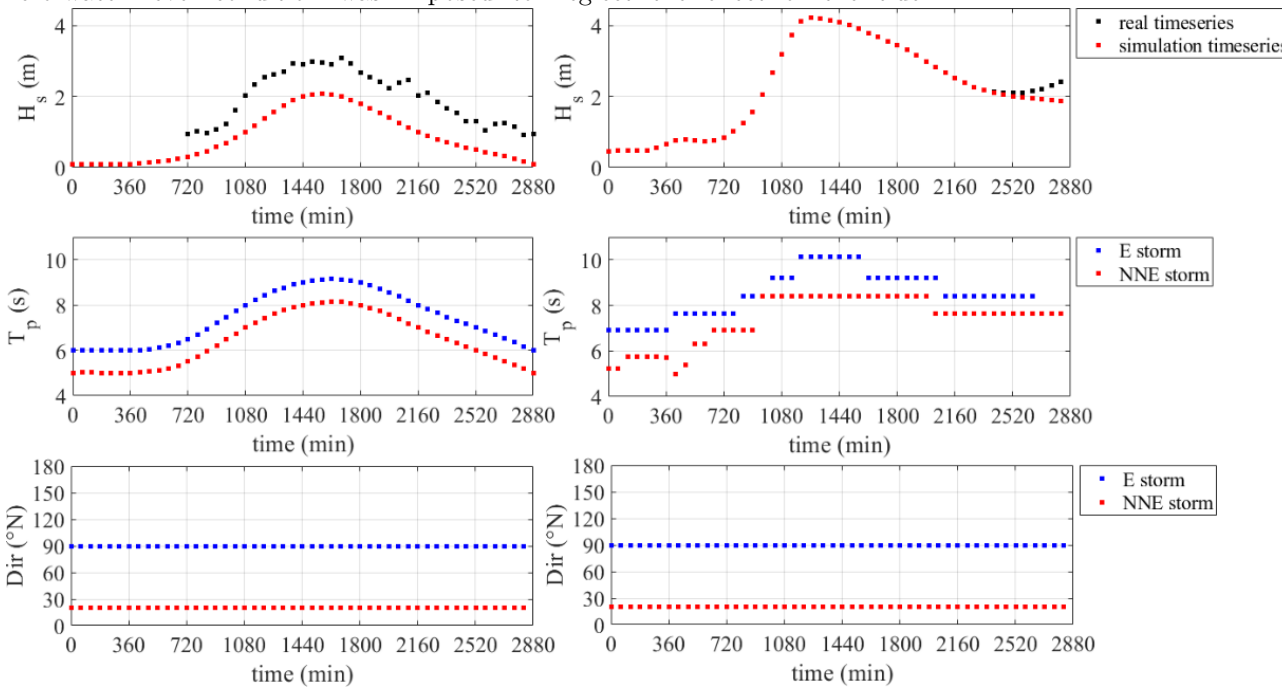

run simulations to verify that both river discharge and waves can suspend sediments inside the river mouth. Thus, we did not add an input concentration in such simulations and only looked at the local generation of the plume. However, we still considered a background concentration of 0.05 kg/m^3 typical of the Northern Adriatic.

We performed three simulations forced only by river discharge timeseries (Sec-

tion 4.1), characterized by discharge peaks of 10 (RD 10), 50 (RD 50) and 100 m^3/s (RD 100) and shape similar to real-life discharge events ("real timeseries"), and four simulations forced only by waves (Section 4.2), characterized by maximum wave heights of 2 and 4 m and by directions equal to 20°N and 90°N (W NNE2, W NNE4, W E2, W E4). Then, we run simulations all forced by the 50 m^3/s river discharge peak but associated with a uniformly distributed and constant wind coming from different directions, to study the effect of the wind on the plume direction (Section 4.3). The wind intensity was fixed at 10 m/s, while the investigated wind directions were 30, 135, 210 and 315°N, to observe the effect of winds directed toward the coast, NW, the offshore and SE, respectively (RD 50 wind 30, RD 50 wind 135, RD 50 wind 210, RD 50 wind 315). We associated the wind also with simulations forced by waves (H_s = 4m), imposing a wind direction in agreement with that of the waves (W NNE4 wind 20, W E4 wind 90). Finally, two simulations were run to inspect the role of high and low tide coupled with the 50 m^3/s river discharge peak (Section 4.4). This was done by creating a sinusoidal timeseries for the tide and by making the peak of the river discharge timeseries simultaneous once with the high tide and once with the low tide (RD 50 ht, RD 50 lt). *Table 2* shows an overview of all the parametric simulations performed.

Table 2. Overview of the parametric simulations.

	USED FORCING			
simulation ID	**river discharge**	**waves**	**wind**	**tide**
RD 10	x	-	-	-
RD 50	x	-	-	-
RD 100	x	-	-	-
W NNE2	-	x	-	-
W NNE4	-	x	-	-
W E2	-	x	-	-
W E4	-	x	-	-
RD 50 wind 30	x	-	x	-
RD 50 wind 135	x	-	x	-
RD 50 wind 210	x	-	x	-
RD 50 wind 315	x	-	x	-
W NNE4 wind 20	-	x	x	-
W E4 wind 90	-	x	x	-
RD 50 ht	x	-	-	x
RD 50 lt	x	-	-	x

4.1 Local resuspension due to river discharge

We simulated three different river discharge hydrographs, with peaks of 10, 50 and 100 m^3/s (see *Figure 14, Table 2*), to find a threshold above which the suspension began. Such threshold was identified as the minimum river discharge

that led to exceeding the model critical shear stress for erosion (0.3 N/m^2). The results of these simulations highlighted that the cohesive concentration composing the plume was an order of magnitude higher than the sand concentration. *Figure 16* shows the cohesive suspended sediment concentration (top row) and the maximum bed shear stress (bottom row), at the time of the discharge peak. The concentration and the maximum bed shear stress were made dimensionless using the representative background concentration for the Northern Adriatic, c_{ref} = 0.05 kg/m^3 and the critical shear stress for erosion, $_{ref}$ = 0.3 N/m^2, respectively. The columns refer to the three river discharge peaks.

The first column shows that the river discharge, until it remained below or equal to 10 m^3/s, could not suspend the sediment, since the critical shear stress for erosion was never exceeded. In cases like this, the only sediment that could form the plume was that eroded in the upstream part of the basin and transported toward the mouth. The simulation characterized by a

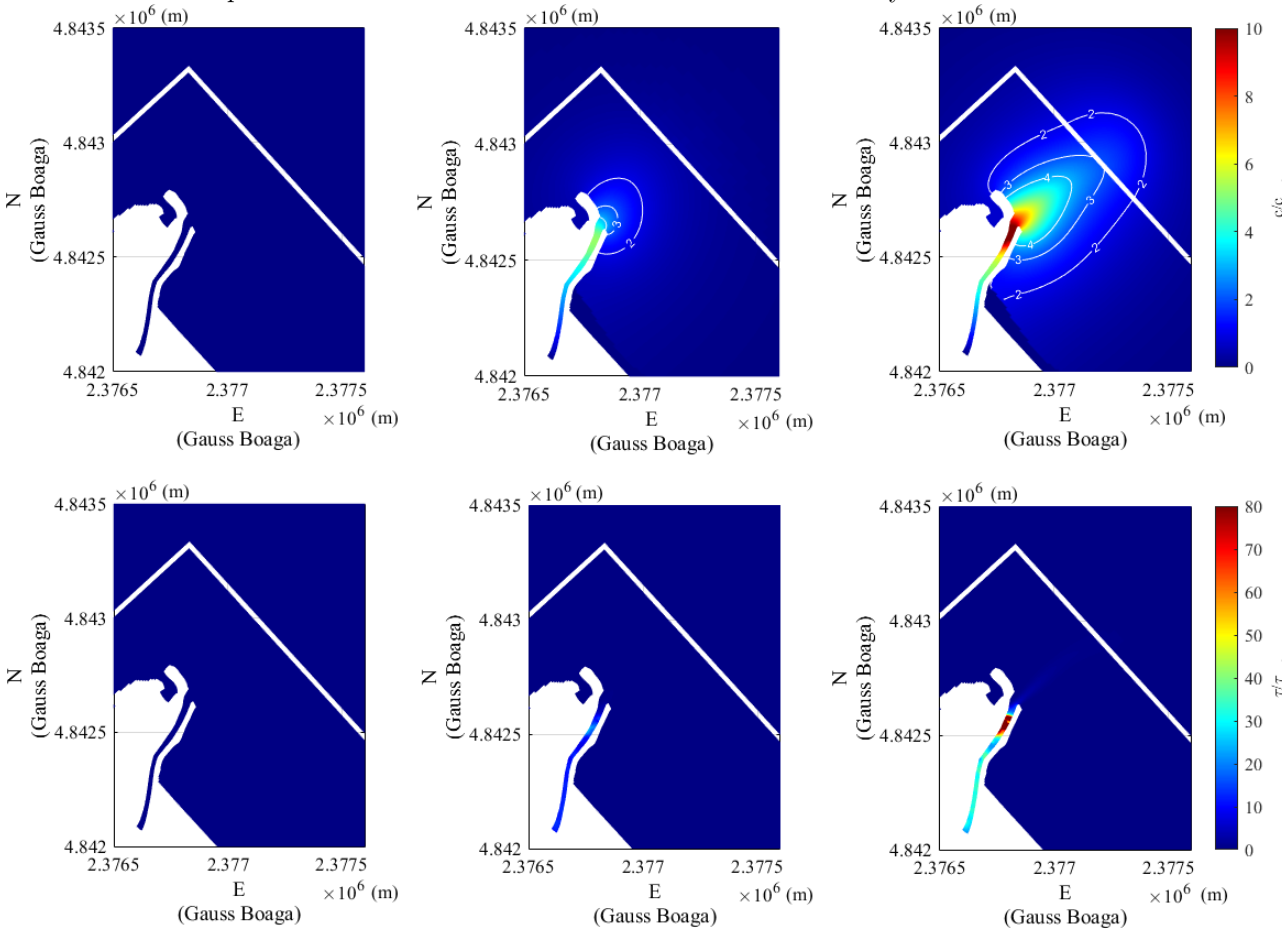

discharge peak of 50 m^3/s allowed us to find the threshold above which the critical shear stress for erosion was exceeded for the first time, which was about

12 m^3/s. The second and third columns show that both the concentration and the shear stress increased when the river discharge increased. The shear stress was maximum in the final reach of the river (red area in the bottom-right panel of *Figure 16*), where the bathymetry was characterized by a large deposit that caused the reduction of the section and the consequent increase of the velocity and of the bed shear stress. At such location, at the peak time, the bed shear stress exceeded the critical one of about 25 times for the 50 m^3/s river discharge peak and 150 times for the 100 m^3/s river discharge peak. Therefore, the maximum suspension due to the river discharge occurred in the final stretch of the river. Here, the concentration was about 5 and 11 times the reference one, respectively for the 50 and 100 m^3/s river discharge peaks.

4.2 Local resuspension due to waves

The wave generation mechanism was studied through four simulations, two forced with NNE waves and two forced with E waves. For each direction, we tested two timeseries, characterized by maximum significant wave height of 2 and 4 m (see *Figure 15, Table 2*). The results showed that the plume was mainly composed by cohesive sediment, while a considerable quantity of sand was resuspended along the coast. To separate the two contributions, we focused on the cohesive fraction. *Figure 17* reports the results in terms of dimensionless cohesive concentration (top row) and maximum bed shear stress (bottom row) at the time of the storm

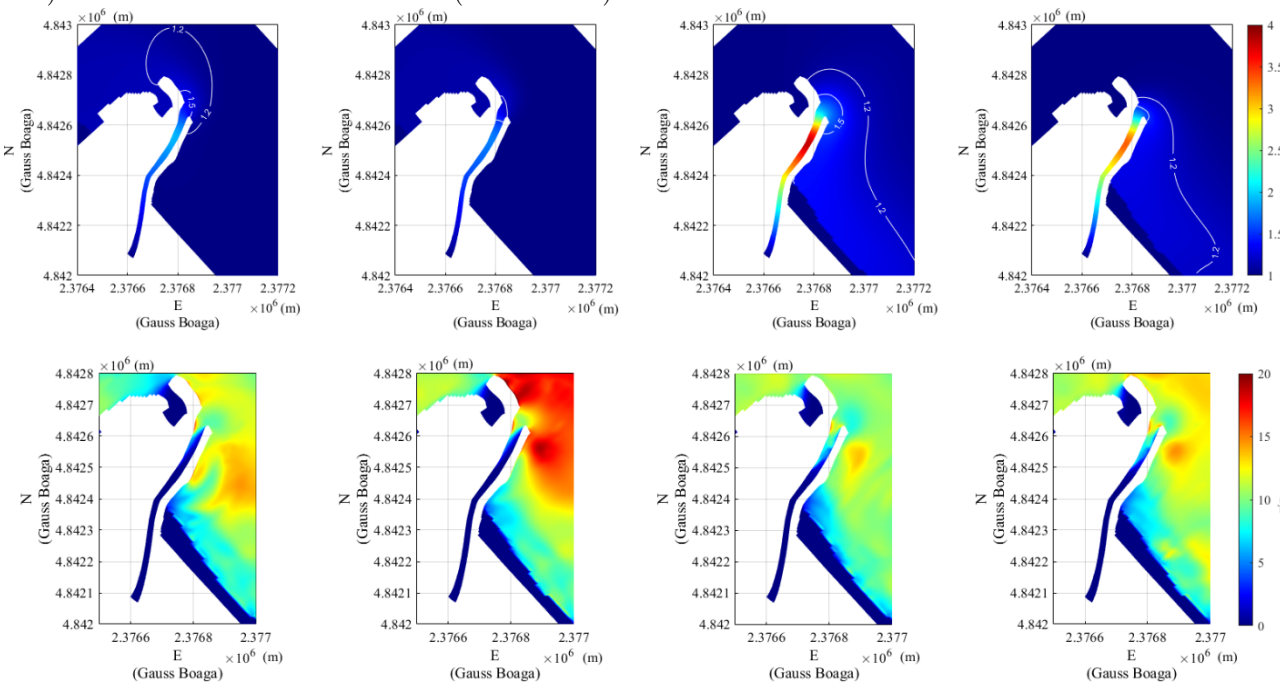

The first and second columns refer to E waves, with $H_{s,max}$ = 2 m and $H_{s,max}$ = 4 m, respectively. The third and fourth columns refer to NNE waves, with

$H_{s,max}$ = 2 m and $H_{s,max}$ = 4 m, respectively.

NNE waves, approaching the coast perpendicularly to the MRE, easily entered the estuary causing the increase of the depth-averaged velocities and of the bed shear stress up to about 190 m upstream from the river mouth. Also E waves could enter the estuary, but to a minor extent, as shown in *Figure 17* (bottom panels). Therefore, the concentration was much higher for the NNE waves. Both NNE and E waves generated a small recirculating cell inside the river mouth, more extended upriver for the NNE waves than for the E waves, with upriver and downriver velocities along the left and right riverbanks, respectively. The intensity of the storm did not greatly affect the magnitude of the bed shear stress inside the river, which was very similar between the simulations characterized by $H_{s,max}$ = 2 m and by $H_{s,max}$ = 4 m. However, a difference existed in the quantity of suspended sediment, being it slightly smaller in the case of $H_{s,max}$ = 4 m. This was due to the fact that the 4 m high storm, during its growth phase, resuspended more sediments than the 2 m storm (which was washed out to sea) and thus, during the peak stage, the available sediments to resuspend were less.

Considering the storm characterized by $H_{s,max}$ = 4 m, comparable with a 10-year return period storm, the shear stress remained below about 12 times the critical stress for both NNE and E waves, apart from a small area near the left riverbank where it reached values about 20 times higher than the critical stress. Therefore, the bed shear stress caused by a 10-year return period storm was about a half than that of the simulation with a 50 m^3/s peak discharge, comparable with a 1-year return period discharge. This means that a river discharge comparable with a 1-year return period river discharge could generate a bed erosion more intense than that triggered by a wave storm comparable with a 10-year return period storm. Thus, the concentration generated by waves reached values equal to 4 times the reference one, i.e. smaller than the concentration resulting from the 50 m^3/s peak discharge simulation. This agrees with the findings of Baldoni et al. (2021), who observed that the migration of the MR inner bar was more affected by river discharges, even if small, rather than intense wave storms.

Numerical simulations confirmed that outside of the MR mouth NNE storms and E storms produced depth-averaged velocities directed, respectively, toward SE and NW, this driving the plume toward such directions. Moreover, the E storm generated an area close to the south pier of the MR, where depth-averaged velocities were directed to the offshore, until they reached the northward flow that developed offshore of the mouth. This suggested that the change of water colour that we observed as due to the ESE waves from the SGS images was caused by wave resuspension along the jetty.

4.3 Effect of the wind

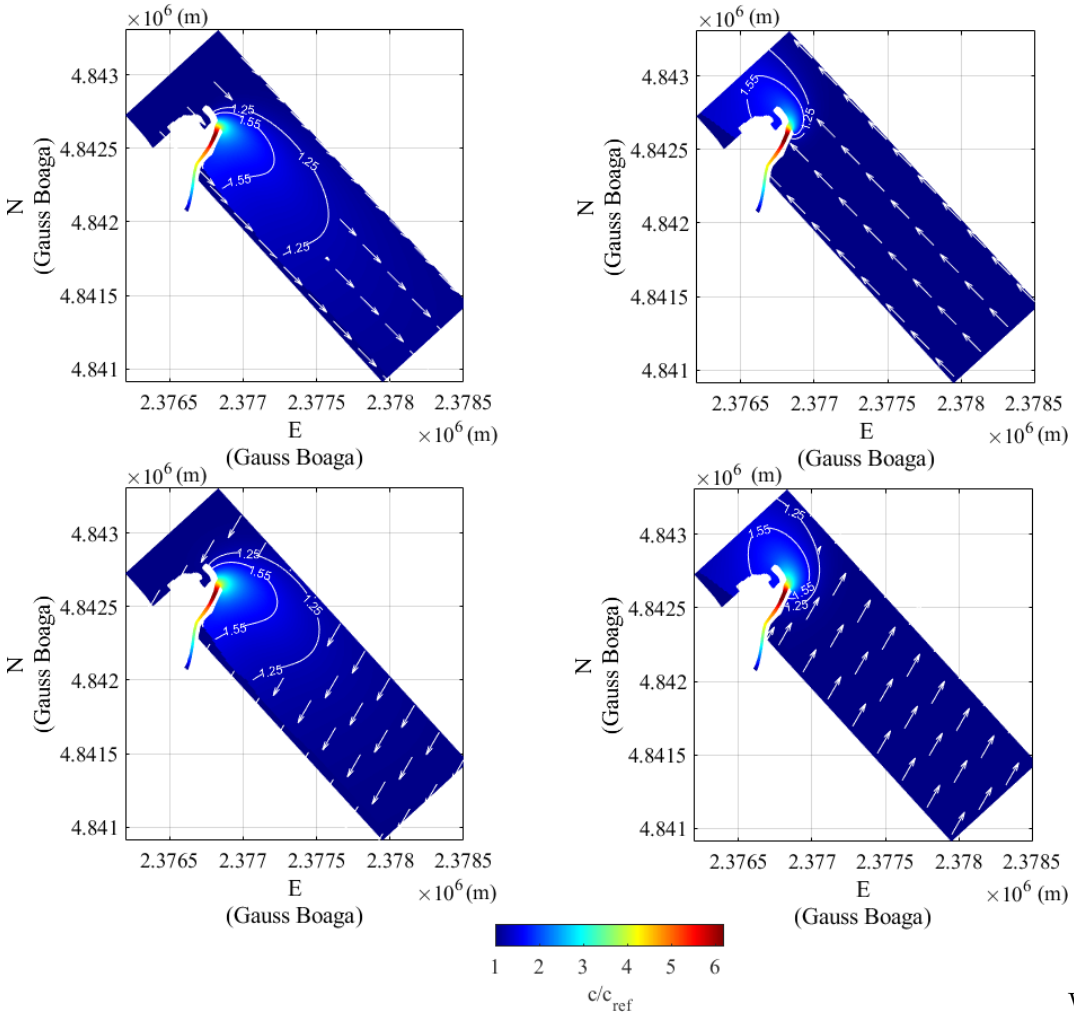

We coupled the simulation characterized by a river discharge peak of 50 m^3/s with winds coming from different directions (*Table 2*). The top panels of *Figure 18* show the results of the simulations forced with winds coming from NW (left panel) and SE (right panel). As expected, the plume was deflected toward SE and NW, respectively. The effect of winds blowing along the final stretch of the river is reported in the bottom panels of *Figure 18*. When the wind blew toward the estuary (left panel), the plume was, again, deviated toward SE, while the wind that was directed toward the sea (right panel) deflected the plume toward NW. This is because both the winds directed inside and outside the estuary had a component along the coastline: the first is directed toward SE, the latter toward NW. Moreover, the higher was the alongshore component of the wind (top panels of *Figure 18*), the smaller was the plume offshore extension, because the plume was strongly and rapidly transported along the coast and did not expand toward the offshore.

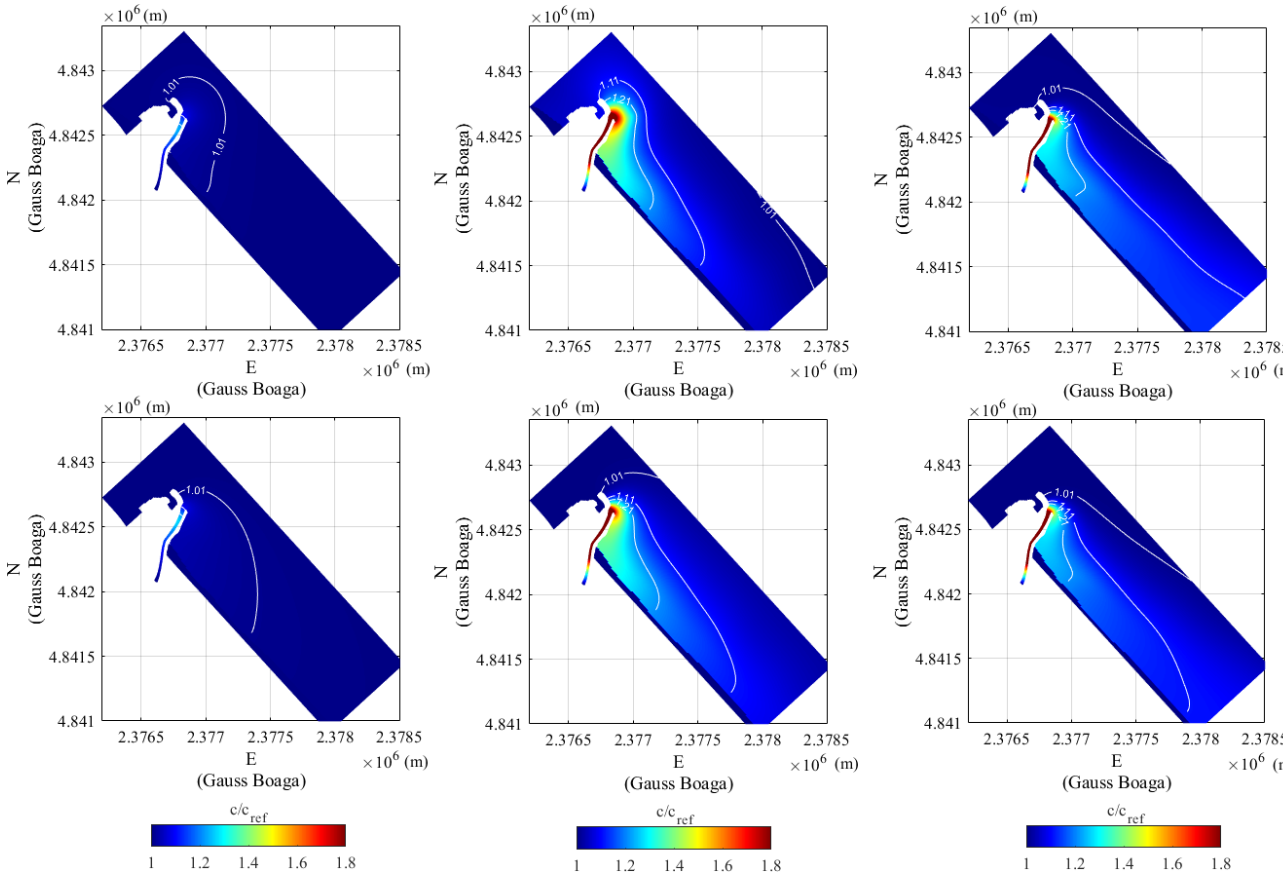

inspect the effect of the wind associated with waves, we coupled the simulation characterized by a maximum significant wave height of 4 m with a wind in agreement with the wave direction (*Table 2*). *Figures 19* and *20* report the results of the simulations forced with NNE and E waves, respectively. For each figure, the top row shows the concentration maps for the simulation run with no wind, while the bottom one shows the results of the simulation run with the wind. The first, second and third columns illustrate the concentrations an instant before the beginning of the storm, an instant during the growth phase of the storm, and the instant of the storm peak, respectively. The colorbars were adjusted to highlight the transport mechanism and the differences between the two wave directions. As already seen, NNE waves penetrated more easily inside the estuary than E waves and resuspended more sediment (*Figures 17*, *19* and *20*).

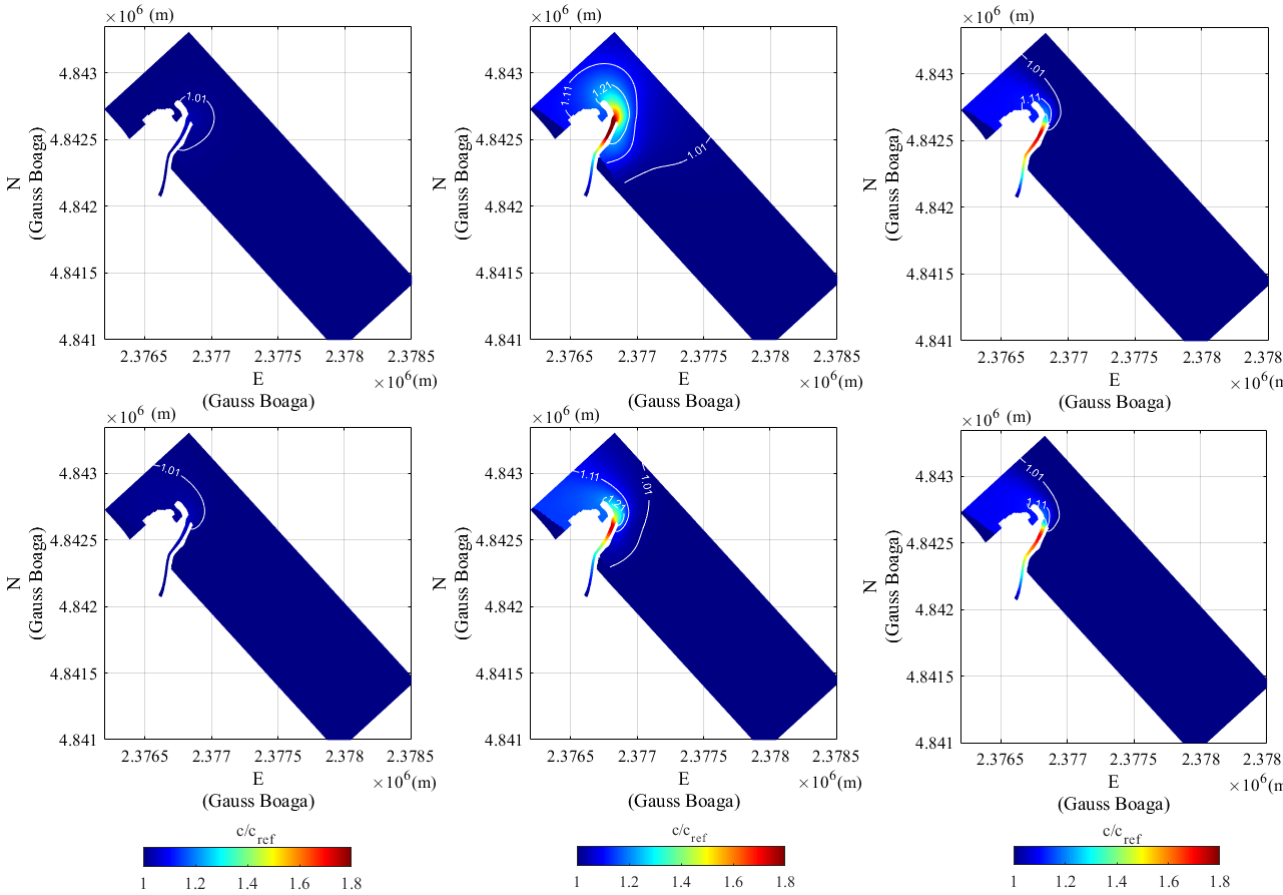

Figure 19 and *Figure 20* and show that, before the storm began (first column), the plume remained around the estuary when the wind was not included in the simulation, while it was deflected toward SE or NW when the wind was associated to NNE and E waves, respectively. During the ascending phase of the storm (second column), even with no wind, the plume started to bend because of the sea currents generated by the waves. From the storm peak (third column) until the end of the simulation, the maps were very similar, suggesting that the currents generated by the storm were the dominant transport mechanism.

4.4 Effect of the tide

The role of the tide in the plume generation and expansion was studied through two simulations where the 50 m^3/s discharge peak was taken to be simultaneous with high and low tide, respectively (*Table 2*). *Figure 21* shows that when the river discharge peak was coincident with the high tide (second column), the suspended concentration was lower than the concentration of the simulation with no tide. This happened because the tidal current opposed the river current and increased the water depth, this reducing the flow velocity (Ruiz-Reina & López-Ruiz, 2021), the bed shear stress and consequently the

suspended sediment concentration and the plume extension. Conversely, if the river discharge occurred concurrently with low tide, the river flow velocity was enhanced, and the water depth decreased (Ruiz-Reina & López-Ruiz,

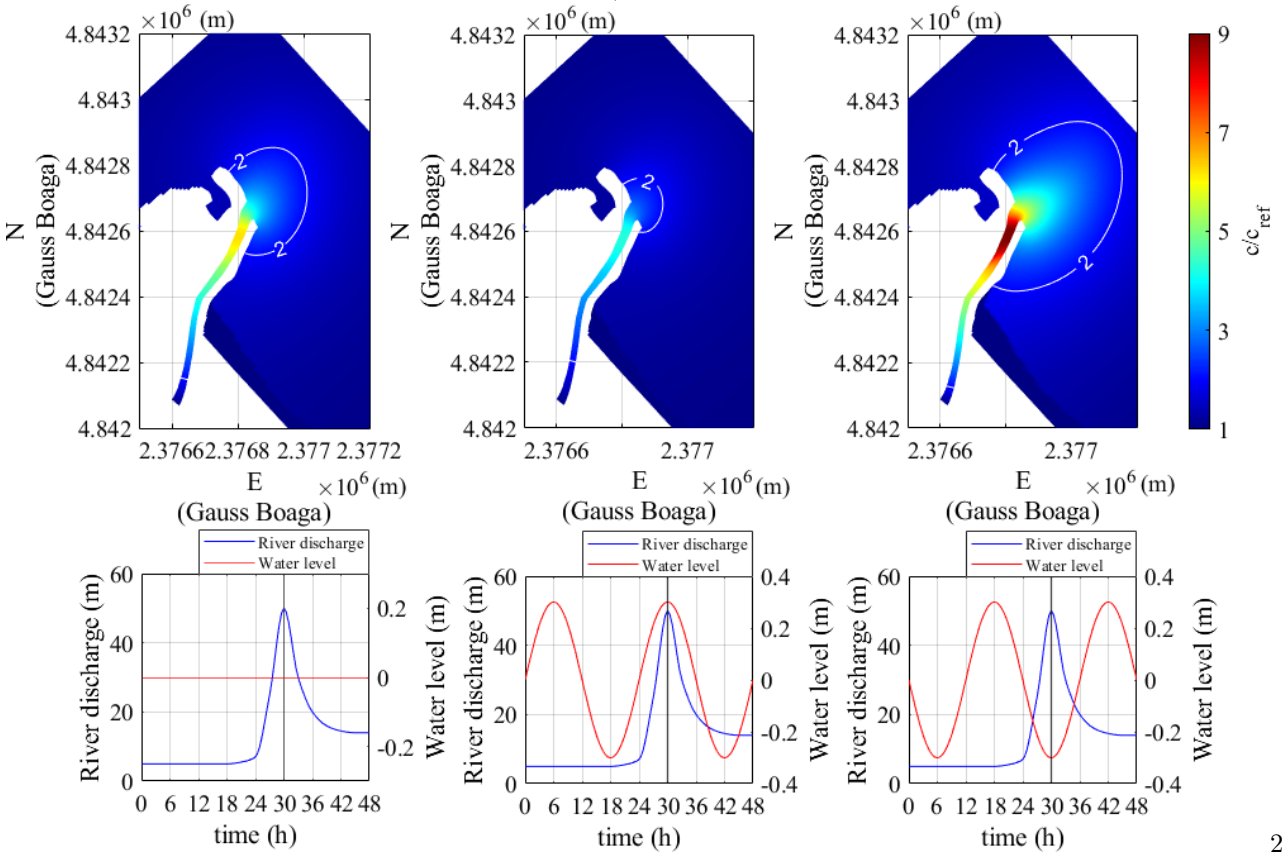

this increasing the suspended concentration and the plume extension with respect to the simulation with no tide. In the simulated cases, we used the maximum tidal range for the MRE (0.6 m), which produced a change in the plume extension (compared with the RD 50 case) of - 65% in the RD 50 ht case and of + 54% in the RD 50 lt case.

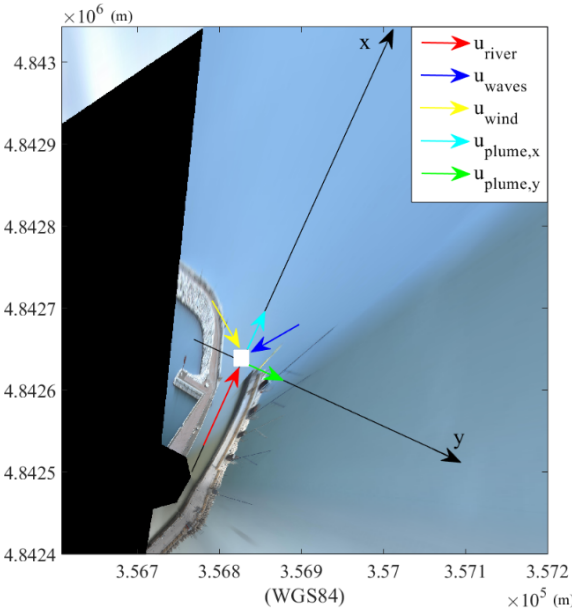

4.5 Extension of the plume

The plume evolution was affected by a combination of factors. We accounted for such interaction by computing a plume surface velocity, u_{plume}, to which we related the plume extension. We considered a reference system with the x-axis directed along the river (*Figure 22*) and we computed the surface velocities due to the river flow, the wind and the waves at the river mouth. We decided to neglect the effect of the tide, even if it could modify the plume extension as shown in Section 4.4 because, for the analysed cases, the tidal excursion was less than ± 0.15 m.

The "PTV velocity" was taken as representative of the river surface velocity, u_{river}, and flowed in the positive x-direction (red arrow in *Figure 22*). The surface water velocity generated by the wind stress, u_{wind}, was related to the wind speed through a factor of 3.2% (Henderson-Sellers, 1988). The surface water velocity due to the wave motion, u_{waves}, was computed as a Stokes drift (van den Bremer & Breivik, 2018), using the Ursell formula valid for general water depths:

$$u_{waves} = c\,(ak)^2 \cosh(2k(h+z))\,/(2\sinh^2(kh)) \quad \text{Eq. 1}$$

where $c = \sqrt{\frac{g}{k}\tanh(kh)}$ is the phase speed, $k = \frac{2\pi}{L}$ is the wave number, $a = \frac{H}{2}$ is the wave amplitude, h is the water depth and z is the vertical coordinate (equal to zero at the free surface). The wave height H at the mouth was available from the Delft3D wave results; the wavelength was computed through the dispersion equation given the water depth and the wave frequency. Both u_{wind} (yellow arrow in *Figure 22*) and u_{waves} (blue arrow in *Figure 22*) were decomposed in the x and y-directions.

Finally, the surface plume velocity components (green and cyan arrows in *Figure*

22) were calculated for all the events in *Table 1* apart from events EV1 and EV9:

$u_{plume,x} = u_{\text{river}} + u_{waves,x} + u_{wind,x}$ Eq. 2

$u_{plume,y} = u_{waves,y} + u_{wind,y}$ Eq. 3

Event EV1 was discarded because it was not possible to track the plume front since it was not visible due to breaking waves. The elaborated video of event EV9 was not in phase with the discharge peak, therefore the plume extension could not be associated with the simultaneous plume velocity.

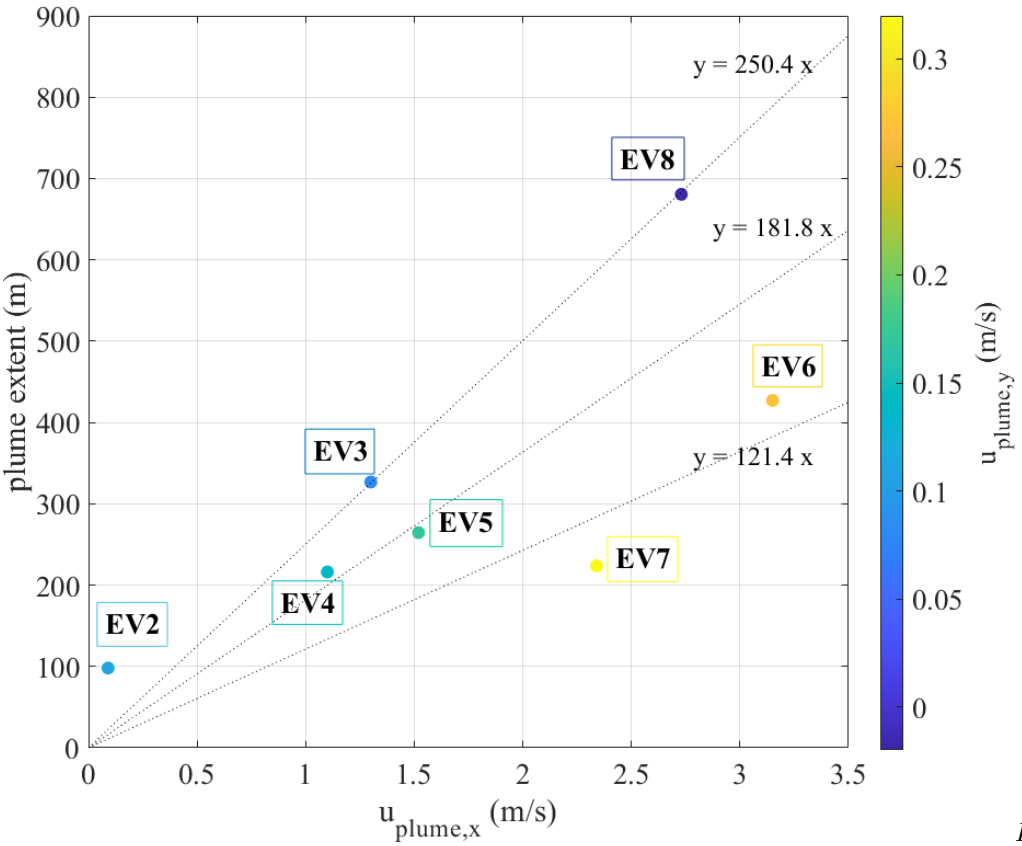

Figure 23 shows the correlation between the plume extent and the plume velocity components. The relation between the plume extension and $u_{plume,x}$ followed a linear law with angular coefficient inversely proportional to $u_{plume,y}$. For similar $u_{plume,y}$, the higher was $u_{plume,x}$ the higher was the plume extension. Such result means that, under similar wave and wind conditions, the plume offshore extension increased with u_{river}. This is in agreement with the findings of Section 4.1, showing that the plume extended more to the offshore at the increase of the river discharge. Plumes characterized by the same $u_{plume,x}$ reached a minor extension when $u_{plume,y}$ increased, because the alongshore current due to waves and wind deviated the plume toward either SE or NW,

limiting its offshore extension (see Section 4.2, Section 4.3). In fact, events EV7 and EV6, characterized by the highest $u_{plume,y}$, fit with the least sloped line, while events EV2, EV3 and EV8, characterized by lower $u_{plume,y}$, fit with the largest sloped line. Moreover, as $u_{plume,y}$ increased, a higher $u_{plume,x}$ was needed to reach the same plume extension. For example, events EV4 and EV7 showed very similar extensions but EV7 needed a larger $u_{plume,x}$ because it was characterized by a stronger $u_{plume,y}$. The magnitude of $u_{plume,y}$ was mainly affected by the wind speed and direction. In fact, refraction makes the wave fronts almost parallel to the coast, this reducing their alongshore component. Therefore, the alongshore velocity increased as due, mainly, to the alongshore component of the wind: winds blowing parallel to the coast caused the smallest plume offshore extensions, as already seen in Section 4.3 (*Figure 18*).

4.6 Supply of sediment to the beach

Both observations and simulations showed that the sediment released by the MR at times contributed to the nourishment of the beaches around the estuary. The geometry of the engineered MR mouth caused the cohesive sediment to exit the MR 300 m offshore from the coast, outside from the breaking zone. The plumes generated by sediment resuspension due to waves were characterized by low sediment concentrations and located near the mouth (*Figures 11, 17*). Such plumes were pushed toward the neighbouring beaches by the incoming waves and contributed to their nourishing. Conversely, the plumes generated by the river current were denser and wider. The parametric RD simulations showed that, in the absence of other forcing, the larger the river discharge the larger the offshore distance reached by the plume and the amount of suspended sediment (*Figure 16*). However, the actual plume evolution was affected by a combination of multiple forcing that transported the sediment along the coast (*Figures 9, 18*). Such interaction reduced the offshore extension of the plume, pushing the sediment toward the breaking zone, while increasing the alongshore one. This sediment dynamics allowed the nourishment also of beaches located far from the MR mouth. The amount of beach supply depended on the quantity of sediment released from the MR, i.e. on the intensity of the generation mechanism (*Figure 6*), while the distance reached by the plume was mainly linked to the strength of the transport mechanisms. Since the plume was mostly directed toward SE, it mainly nourished the beach south of the MRE.

5 Conclusions

The complex estuarine morpho-hydrodynamics is characterized by the interaction of multiple forcing. The study of the MR plume through images, numerical simulations and PTV analyses allowed us to identify two local generation mechanisms (Section 3.1) and two main transport mechanisms (Section 3.2).

The most intense and extended plumes occurred during river discharges events due to both local resuspended sediment and material supplied by the river flow from the upper part of the watershed (*Figure 6a, Figure 9*). Therefore, these plume events released the largest amount of sediment that, based on the trans-

port mechanisms, nourished close or far beaches.

Parametric simulations showed that river discharges higher than 12 m^3/s were able to resuspend the sediment and that the plume offshore extension and concentration increased with the river discharge (*Figure 16*). PTV analyses highlighted the direct proportionality between the river flow rate and the river surface velocity (*Figure 13*). Moreover, being such velocity mainly directed toward the open sea, it influenced only the offshore expansion.

The waves were another local generation mechanism and they were also responsible for the sediment transport. Plume events caused by waves were less dense than plumes generated by the river discharge. Real-life simulations highlighted that the concentration isoline followed by the observed plume front of the RD case (0.1 kg/m^3) was about twice the isoline corresponding to the front of the W case (0.059 kg/m^3). Furthermore, the parametric simulations confirmed that 10-year return period waves, resuspended less sediment than a 1-year return period river discharge.

The wave action, opposing the river flow, kept the plume near the mouth (*Figure 6b, Figure 11*) and contributed to the supply of sediment to adjacent beaches. In addition, oblique incoming waves deflected the plume along the coast, allowing the nourishment of farther beaches. Such alongshore transport was enhanced by the wind (*Figure 19*, *Figure 20*). Actually, the wind was the main transport mechanism and the major component of the alongshore plume surface velocity. The larger was such alongshore velocity, the more the plume was pushed along the coast reducing its offshore extension. Instead, the sediment expansion toward the sea was linearly proportional to the along-river plume velocity, with angular coefficient inversely proportional to the alongshore plume velocity (*Figure 23*).

Finally, we observed that the tide could affect both the concentration and the extension of the plume when the tidal excursion was set equal to the maximum tidal range for MRE (*Figure 21*). However, in most common cases the tide could be neglected in comparison to the other mechanisms.

Acknowledgments

The financial support from the Office of Naval Research Global (UK) MORSE Project (Research Grant N62909-17-1-2148) and from the Fondazione Cariverona 2019 PhD scholarship "Osservazione e MODellazione dell'idromorfoDINamica estuarina e costiera (OSMODIN)" (2019.0294 - D.R. n. 603 of May 28, 2019) is gratefully acknowledged. The authors would like to thank their colleagues who made significant contributions for both the field experiment and use of the SGS station, including Luciano Soldini, Joe Calantoni, Edward F. Braithwaite III, Alex Sheremet, Allen Reed, Margaret L. Palmsten. Additionally, the authors would like to thank the following authorities: the Municipality of Senigallia, the Capitaneria di Porto of Senigallia and of Ancona. Acknowledgments go also to: Civil Protection – Marche Region, Multi-risk Functional Center, GESTIPORT (Senigallia), Club Nautico (Senigallia), NOTA

srl (Senigallia), Carmar Sub (Ancona), Sena Gallica (Senigallia), METIS S.R.L. (Senigallia).

Open Research

Inputs for the numerical simulations, datasets and a script for the pre-processing of the images for PTV analyses are available at the following Zenodo repository: https://doi.org/10.5281/zenodo.5595957

References

AQUATER - REGIONE MARCHE (1982) – Studio Generale per la difesa delle coste. Prima fase. Vol. II: rapporto di settore.

Arnoux-Chiavassa, S., Rey, V., & Fraunie, P. (1999). Modelling of suspended sediment fluxes off the Rhone River mouth. *Journal of coastal research*, 61-73. https://www.jstor.org/stable/4298915

Baldoni, A., Perugini, E., Soldini, L., Calantoni, J., & Brocchini, M. (2021). Long-term evolution of an inner bar at the mouth of a microtidal river. *Estuarine, Coastal and Shelf Science*, 107573. https://doi.org/10.1016/j.ecss.2021.107573

Banas, N. S., MacCready, P., & Hickey, B. M. (2009). The Columbia River plume as cross-shelf exporter and along-coast barrier. *Continental Shelf Research*, 29(1), 292-301. https://doi.org/10.1016/j.csr.2008.03.011

Bourrin, F., Friend, P. L., Amos, C. L., Manca, E., Ulses, C., Palanques, A., Durrieu de Madron, X., & Thompson, C. E. L. (2008). Sediment dispersal from a typical Mediterranean flood: the Têt River, Gulf of Lions. *Continental Shelf Research*, 28(15), 1895-1910. https://doi.org/10.1016/j.csr.2008.06.005

Brando, V. E., Braga, F., Zaggia, L., Giardino, C., Bresciani, M., Matta, E., ... & Carniel, S. (2015). High-resolution satellite turbidity and sea surface temperature observations of river plume interactions during a significant flood event. *Ocean Science*, 11(6), 909-920.

Brocchini, M., Calantoni, J., Postacchini, M., Sheremet, A., Staples, T., Smith, J., Reed, A.H., BraithwaiteIII, E.F., Lorenzoni, C., Russo, A., Corvaro, S., Mancinelli, A. & Soldini, L. (2017). Comparison between the wintertime and summertime dynamics of the Misa River estuary. *Marine Geology*, 385, 27-40. https://doi.org/10.1016/j.margeo.2016.12.005

Broche, P., Devenon, J. L., Forget, P., de Maistre, J. C., Naudin, J. J., & Cauwet, G. (1998). Experimental study of the Rhone plume. Part I: physics and dynamics. *Oceanologica acta*, 21(6), 725-738. https://doi.org/10.1016/S0399-1784(99)80002-4

Chao, S.-Y. (1987). Wind-driven motion near inner shelf fronts. *Journal of Geophysical Research*, 92, 3849-3860. https://doi.org/10.1029/JC092iC04p0384

Chao, S.-Y. (1988). Wind-driven motion of estuarine plumes. *Journal of Physical Oceanography*, 18, 1144-1166. https://doi.org/10.1175/1520-0485(1988)018%3C1144:WDMOEP%3E2.0.CO;2

Darvini, G., & Memmola, F. (2020). Assessment of the impact of climate variability and human activities on the runoff in five catchments of the Adriatic Coast of south-central Italy. *Journal of Hydrology: Regional Studies*, 31, 100712. https://doi.org/10.1016/j.ejrh.2020.100712

de Boer, G. J., Pietrzak, J. D., & Winterwerp, J. C. (2009). SST observations of upwelling induced by tidal straining in the Rhine ROFI. *Continental Shelf Research*, 29(1), 263-277. https://doi.org/10.1016/j.csr.2007.06.011

Deltares, 2014. Delft3D-Flow, Simulation of multi-dimensional hydrodynamic flows and transport phenomena, including sediments, User Manual, Version 3.15.34158, May 2014, 684 pp.

Deltares, 2019. Delft3D-Wave, Simulation of short-crested waves with SWAN, User Manual, Version 3.05.58426, May 2019, 200 pp.

Dinamica della sedimentazione marina e impatto sulla costa.pdf (Regione Marche)

Favali, P., Frugoni, F., Monna, D., Rainone, M. L., Signanini, P., & Smriglio, G. (1995). The 1930 earthquake and the town of Senigallia (Central Italy): an approach to seismic risk evaluation. *Annals of Geophysics*, 38(5-6).

Fong, D. A., & Geyer, W. R. (2001). Response of a river plume during an upwelling favorable wind event. *Journal of Geophysical Research: Oceans*, 106(C1), 1067-1084. https://doi.org/10.1029/2000JC900134

Frignani, M., Langone, L., Ravaioli, M., Sorgente, D., Alvisi, F., & Albertazzi, S. (2005). Fine-sediment mass balance in the western Adriatic continental shelf over a century time scale. *Marine Geology*, 222, 113-133. https://doi.org/10.1016/j.margeo.2005.06.016

Garvine, R. W. (1995). A dynamical system for classifying buoyant coastal discharges. *Continental Shelf Research*, 15(13), 1585-1596. https://doi.org/10.1016/0278-4343(94)00065-U

Garvine, R. W. (1999). Penetration of Buoyant Coastal Discharge onto Continental Shelf: A Numerical Model Experiment. *Journal of Physical Oceanography*, 29(8), 1892-1909. https://doi.org/10.1175/1520-0485(1999)029%3C1892:POBCDO%3E2.0.CO;2

Grilli, F., Marini, M., Degobbis, D., Ferrari, C. R., Fornasiero, P., Russo, A., Gismondi, M., Djakovac, T., Precali, R., & Simonetti, R. (2005). Circulation and horizontal fluxes in the northern Adriatic Sea in the period June 1999–July

2002. Part II: Nutrients transport. Science of the total environment, 353(1-3), 115-125. https://doi.org/10.1016/j.scitotenv.2005.09.011

Henderson-Sellers, B. (1988). The dependence of surface velocity in water bodies on wind velocity and latitude. *Applied mathematical modelling*, 12(2), 202-203. https://doi.org/10.1016/0307-904X(88)90012-1

Harris, C. K., Sherwood, C. R., Signell, R. P., Bever, A. J., & Warner, J. C. (2008). Sediment dispersal in the northwestern Adriatic Sea. *Journal of Geophysical Research: Oceans*, 113(C11). https://doi.org/10.1029/2006JC003868

Hessner, K., Rubino, A., Brandt, P., & Alpers, W. (2001). The Rhine outflow plume studied by the analysis of synthetic aperture radar data and numerical simulations. *Journal of physical oceanography*, 31(10), 3030-3044. https://doi.org/10.1175/1520-0485(2001)031%3C3030:TROPSB%3E2.0.CO;2

Janke, T., Schwarze, R., & Bauer, K. (2020). Part2Track: A MATLAB package for double frame and time resolved Particle Tracking Velocimetry. SoftwareX, 11, 100413. https://doi.org/10.1016/j.softx.2020.100413

Korres, G., Ravdas, M., & Zacharioudaki, A. (2019). Mediterranean Sea waves analysis and forecast (CMEMS MED-Waves).

Lee, H. J. & Liu, K. K. (2013). Tidal effects on Changjiang plume dispersal in the East China Sea. *Journal of Marine Science and Technology*, 21(3), 342-352. 10.6119/JMST-013-0207-1

Lesser, G., Roelvink, J., Van Kester, J., Stelling, G., 2004. Development and validation of a three-dimensional morphological model. *Coastal Engineering*, 51, 883–915.

Lentz, S. J., & Largier, J. (2006). The influence of wind forcing on the Chesapeake Bay buoyant coastal current. *Journal of Physical Oceanography*, 36(7), 1305-1316. https://doi.org/10.1175/JPO2909.1

Li, M., & Rong, Z. (2012). Effects of tides on freshwater and volume transports in the Changjiang River plume. *Journal of Geophysical Research: Oceans*, 117(C6). https://doi.org/10.1029/2011JC007716

Liedtke, J., Roberts, A., & Luternauer, J. (1995). Practical remote sensing of suspended sediment concentration. *Photogrammetric engineering and remote sensing*, 61(2), 167-175.

Melito, L., Parlagreco, L., Perugini, E., Postacchini, M., Devoti, S., Soldini, L., Zitti, G., Liberti, L. & Brocchini, M. (2020). Sandbar dynamics in microtidal environments: Migration patterns in unprotected and bounded beaches. *Coastal Engineering*, 161, 103768. https://doi.org/10.1016/j.coastaleng.2020.103768

Mestres, M., Sierra, J. P., & Sánchez-Arcilla, A. (2007). Factors influencing the spreading of a low-discharge river plume. *Continental Shelf Research*, 27(16),

2116-2134. https://doi.org/10.1016/j.csr.2007.05.008

Milliman, J. D., & Syvitski, J. P. (1992). Geomorphic/tectonic control of sediment discharge to the ocean: the importance of small mountainous rivers. *The journal of Geology*, 100(5), 525-544. https://doi.org/10.1086/629606

Morichon, D., Dailloux, D., Aarninkhof, S., & Abadie, S. (2008). Using a shore-based video system to hourly monitor storm water plumes (Adour River, Bay of Biscay). *Journal of Coastal Research*, (24), 133-140. https://doi.org/10.2112/06-0705.1

Naudin, J. J., Cauwet, G., Chretiennot-Dinet, M. J., Deniaux, B., Devenon, J. L., & Pauc, H. (1997). River discharge and wind influence upon particulate transfer at the land–ocean interaction: case study of the Rhone River plume. *Estuarine, Coastal and Shelf Science*, 45(3), 303-316. https://doi.org/10.1006/ecss.1996.0190

Osadchiev, A., & Zavialov, P. (2019). Structure and dynamics of plumes generated by small rivers. In: *Estuaries and Coastal Zones-Dynamics and Response to Environmental Changes*. IntechOpen.

Osadchiev, A., Barymova, A., Sedakov, R., Zhiba, R., & Dbar, R. (2020). Spatial structure, short-temporal variability, and dynamical features of small river plumes as observed by aerial drones: case study of the Kodor and Bzyp river plumes. *Remote Sensing*, 12(18), 3079. https://doi.org/10.3390/rs12183079

Parlagreco, L., Melito, L., Devoti, S., Perugini, E., Soldini, L., Zitti, G., & Brocchini, M. (2019). Monitoring for coastal resilience: preliminary data from five Italian sandy beaches. *Sensors*, 19(8), 1854. https://doi.org/10.3390/s19081854

Perugini, E., Soldini, L., Palmsten, M., Calantoni, J., Brocchini, M. (2018). A new video monitoring station along the Adriatic Coast. XXXVI Convegno Nazionale di Idraulica e Costruzioni Idrauliche, IDRA2018, Ancona, Italy, 12-14 September 2018.

Perugini, E., Soldini, L., Palmsten, M.L., Calantoni, J., Brocchini, M. (2019). Linear depth inversion sensitivity to wave viewing angle using synthetic optical video. *Coastal Engineering*, 152. https://doi.org/10.1016/j.coastaleng.2019.103535

Pigorini, B. (1968). Sources and dispersion of recent sediments of the Adriatic Sea. *Marine Geology*, 6(3), 187-229. https://doi.org/10.1016/0025-3227(68)90031-5

Postacchini, M., Soldini, L., Lorenzoni, C., & Mancinelli, A. (2017). Medium-term dynamics of a middle Adriatic barred beach. *Ocean Science*, 13(5), 719-734. https://doi.org/10.5194/os-13-719-2017

Postacchini, M., Manning, A.J., Calantoni, J., Smith, J.P. & Brocchini, M. (2021). A Storm Driven Turbidity Maximum in a Microtidal Estuary. *Journal*

of Geophysical Research – Oceans (under peer review).

Ravaioli, M., Bergami, C., Riminucci, F., Aracri, S., Aliani, S., Bastianini, M., Bergamasco, A., Bommarito, C., Borghini, M., Bozzano, R., Cantoni, C., Caterini, E., Cardin, V., Cesarini, C., Colucci, R.R., Crisafi, E., Crise, A., D'Adamo, R., Fanara, C., Giorgetti, A., Grilli, F., Langone, L., Lipizer, M., Marini, M., Menegon, S., Minuzzo, T., Miserocchi, S., Partescano, E., Paschini, E., Pavesi, F., Penna, P., Pensieri, S., Pugnetti, A., Raicich, F., di Sarra, A.G., Sarretta, A., Schroeder, K., Stanghellini, G., Vetrano, A. (2017). La rete scientifica italiana di siti fissi per l'osservazione del mare – IFON Stato dell'arte e upgrades durante il Progetto RITMARE (2012 – 2016). A cura di: Ravaioli M., Bergami C., Riminucci F. (2017). Roma, CNR Pubblicazioni 2017. pp. 50, ISBN 978-88-80802-44-0 (online [accessed Apr 02 2021]).

Rolandi, G., Paone, A., Di Lascio, M., & Stefani, G. (2008). The 79 AD eruption of Somma: The relationship between the date of the eruption and the southeast tephra dispersion. *Journal of Volcanology and Geothermal Research*, 169(1-2), 87-98. https://doi.org/10.1016/j.jvolgeores.2007.08.020

Ruiz-Reina, A., & López-Ruiz, A. (2021). Short-term river mouth bar development during extreme river discharge events: The role of the phase difference between the peak discharge and the tidal level. *Coastal Engineering*, 103982. https://doi.org/10.1016/j.coastaleng.2021.103982

Simpson, J. H., Bos, W. G., Schirmer, F., Souza, A. J., Rippeth, T. P., Jones, S. E., & Hydes, D. (1993). Periodic stratification in the Rhine ROFI in the north-sea. *Oceanologica Acta*, 16(1), 23-32. https://archimer.ifremer.fr/doc/00099/21050/

Soosaar, E., Maljutenko, I., Uiboupin, R., Skudra, M., & Raudsepp, U. (2016). River bulge evolution and dynamics in a non-tidal sea-Daugava River plume in the Gulf of Riga, Baltic Sea. *Ocean Science*, 12(2). https://doi.org/10.5194/os-12-417-2016

Van Den Bremer, T. S., & Breivik, Ø. (2018). Stokes drift. *Philosophical Transactions of the Royal Society A: Mathematical, Physical and Engineering Sciences*, 376(2111), 20170104. https://doi.org/10.1098/rsta.2017.0104

Visser, A. W., Souza, A. J., Hessner, K., & Simpson, J. H. (1994). The effect of stratification on tidal current profiles in a region of fresh-water influence. *Oceanologica acta*, 17(4), 369-381. https://archimer.ifremer.fr/doc/00098/20898/

Yankovsky, A. E., & Chapman, D. C. (1997). A Simple Theory for the Fate of Buoyant Coastal Discharges, *Journal of Physical Oceanography*, 27(7), 1386-1401. https://journals.ametsoc.org/view/journals/phoc/27/7/1520-0485_1997_027_1386_astftf_2.0.co_2.xml